Universidade de Aveiro
Ano 2016/2017
Departamento de Física

José Miguel Pino Gonçalves

Elétrodos de grafeno induzido por laser para desionização capacitiva.

Laser-induced graphene electrodes for capacitive deionization.

Universidade de Aveiro
Ano 2016/2017

Departamento de Física

José Miguel Pino Gonçalves

Elétrodos de grafeno induzido por laser para desionização capacitiva.

Laser-induced graphene electrodes for capacitive deionization.

Dissertação apresentada à Universidade de Aveiro para cumprimento dos requisitos necessários à obtenção do grau de Mestre em Engenharia Física realizada sob a orientação científica da Professora Doutora Florinda Mendes da Costa, Professora Associada do Departamento de Física da Universidade de Aveiro, do Dr. António José Silva Fernandes, Técnico Superior do Departamento de Física da Universidade de Aveiro. Este trabalho foi realizado em parceira com a empresa Bosch Termotecnologia S.A. Aveiro, sob a supervisão da Doutora Alexandra Gonçalves.

O presente estudo foi realizado no âmbito do Projeto Smart Green Homes [POCI-01-0247-FEDER-007678], desenvolvido em co-promoção entre a Bosch Termotecnologia S.A. e a Universidade de Aveiro. É financiado pelo Portugal 2020, no âmbito do Programa Operacional Competitividade e Internacionalização, e pelo Fundo Europeu de Desenvolvimento Regional.

Cofinanciado por:

COMPETE 2020 PORTUGAL 2020 UNIÃO EUROPEIA Fundo Europeu de Desenvolvimento Regional

Dedico este trabalho à minha família.

o júri

presidente	Prof.ª Doutora Margarida Maria Resende Vieira Facão Professora auxiliar do Departamento de Física da Universidade de Aveiro
orientadora	Prof.ª Doutora Florinda Mendes da Costa Professora associada do Departamento de Física da Universidade de Aveiro
arguente	Prof. Doutor Victor Fernando Santos Neto Professor auxiliar convidado do Departamento de Mecânica da Universidade de Aveiro

agradecimentos

Primeiramente, agradeço à Professora Doutora Florinda da Costa e ao Dr. António Fernandes Silva Fernandes, por todo o apoio e orientação dado ao longo deste trabalho.

Estendo também o meu agradecimento à Doutora Alexandra Gonçalves, assim como à Bosch Termotecnologia S.A. Aveiro por todo o apoio dado na realização desta tese.

Ao Alexandre e à Joana, um enorme obrigado por todo o tempo e paciência dispensados para esclarecer e ajudar a resolver os mais diversos problemas e despistes experimentais.

A todo o grupo das mesas ao sol do primeiro piso do Departamento de Física, um enorme agradecimento por todas as aventuras pelas ruas de Aveiro, pela companhia em tantas noitadas no Departamento e pelas amizades que para sempre ficarão, em especial ao argentino.

Por último, aos meus pais, agradeço por tudo sempre terem feito para providenciar todas as ferramentas para perseguir os meus objetivos.

palavras-chave CDI, LIG, grafeno, elétrodo, desionização capacitiva

resumo

Este trabalho tem como objetivo a síntese de elétrodos à base de grafeno induzido por laser (LIG) para serem explorados pela primeira vez num sistema de desionização capacitiva (CDI) para remoção de iões da água. O trabalho foi desenvolvido em colaboração com a Bosch Termotecnologia S.A. Aveiro no âmbito de um projeto em Co-promoção.

A síntese dos elétrodos de LIG foi realizada utilizando um polímero comercial, Kapton, sobre o qual se fez incidir um feixe laser de CO_2. O trabalho focou-se no estudo da influência de vários parâmetros de processamento a laser para a otimização dos elétrodos. A caracterização do material foi feita usando as técnicas de microscopia eletrónica de varrimento (SEM), medição da superfície específica (BET), espectroscopia de Raman, medidas de resistência elétrica pela técnica de Van der Pauw e testes de estabilidade em fluxo de água. Paralelamente a este estudo foram também caracterizados quatro elétrodos comerciais.

Para a caracterização dos elétrodos foi desenvolvido um sistema que permite avaliar o comportamento no processo de desionização capacitiva nos modos de corrente (CC) e tensão (CV) constantes. O desempenho do material desenvolvido foi avaliado através da análise de ciclos de carga/descarga, e comparado com o comportamento dos dois melhores elétrodos comerciais.

Os testes realizados permitiram observar a operação de CDI em todos os elétrodos, embora com diferentes níveis de desempenho. Os elétrodos de LIG revelaram uma curva de carga/descarga tipicamente capacitiva, não obstante o seu desempenho ser inferior aos elétrodos comerciais. Os resultados obtidos neste estudo exploratório, aliados ao método de produção a laser de baixo custo, põem em evidência o potencial destes elétrodos para uma aplicação CDI industrial requerendo, no entanto, a sua otimização.

keywords CDI, LIG, graphene, electrode, capacitive deionization

abstract

The goal of this work is the synthesis of electrodes based on laser induced graphene (LIG) to be explored for the first time in a capacitive deionization (CDI) system for ion removal from water. The work was developed in cooperation with Bosch Thermotechnology S.A Aveiro in the ambit of a project in Co-promotion.
The LIG's electrodes synthesis was done using a commercial polymer, Kapton, in which a CO_2 laser beam was irradiated. The work focused on the study of the influence of various laser processing parameters for the optimization of the electrodes. The characterization of the material was done using techniques such as scanning electron microscopy (SEM), specific surface adsorption measurements (BET), Raman spectroscopy, Van der Pauw electrical resistance sheet measurements and stability tests in the presence of a water flow. In parallel with this study, four commercial electrodes were also characterized.
For the characterization of the electrodes was developed a system which allowed to evaluate their behaviour in the process of capacitive deionization in the operation modes of constant current (CC) and voltage (CV). The performance of the developed material was assessed via the analysis of the charge/discharge cycles, and comparing them to the behaviour of two other commercial electrodes. The test executed showed the CDI operation in all of the electrodes, although with different levels of performance. The LIG electrodes revealed a charge/discharge curve typically capacitive, regardless of showing inferior performance results compared to the commercial electrodes. The results obtained in this exploratory work, allied to the LIG's electrode production at low cost, evidences the potential of these electrodes for an industrial CDI application requiring, however, further optimization.

Content

Figure List

Table list

1. Introduction

The scarcity of water is regarded as the second biggest problem of humanity for the next fifty years according to Richard E. Smalley (1943-2005), 1996 Chemistry Nobel Prize winner. Nowadays, the demand for freshwater has been increasing at a remarkable pace, as a result of the ever-growing world's population [1,2]. Even though the global water supplies exceed 1.38×10^{9} km^3, only 2.5% of it is freshwater. Furthermore, less than 1.2% of all freshwater is available for human needs, since the remaining percentage is inaccessible, either in the form of icebergs or underground water [3]. For these reasons, the availability of affordable freshwater is one of the key technological, social and economical challenges of the twenty first century [4], which propels the development of water desalination processes such as reverse osmosis (RO) [5], multi stage flash (MSF) [6], mechanical vapor compression (MVC) [7], multi effect evaporation (MED) [8] and electrodialysis (ED) [9], among others. However, these processes are not ideal, due to their high energy consumption, initial investment and maintenance [10]. A summary of the main features of these techniques is depicted in Table 1.

Table 1: Comparison between several desalination technologies.

Desalination technology	RO	MSF	MVC	MED	ED	CDI
Energy Requirement	2.9-3.7 kWh/m^3 [9]	4 kWh/m^3 [9]	10-14 kWh/m^3 [8]	4.5 kWh/m^3 [8]	2.03 kWh/m^3 [1]	0.5-1.5 kWh/m^3 [11]
Strengths	Well established [1]	Well established [1]	High process efficiency [8]	Operates at low top brine temperatures between 60-70ºC [8]	Waste water treatment as well as brackish water [12]	Low pressure [9]
Weakness	Needs multiple stages for water recoveries over 40% [5]	Requires optimal operation conditions [13]	Requires optimal operation conditions [13]	Very small unit capacity [8]	Needs feed pre-treatment [9]	Seawater desalination is difficult [1]
Economical Cost	Low [1]	High [1]	High	High [1]	High [1]	Low [1]

Consequently, the scientific community has been focusing their efforts into developing environmentally friendly methods, as well as economically viable. For these reasons, capacitive deionization (CDI) has earned the interest of scientists since its theoretical basis was first introduced by Blair, Murphy and co-workers through the 1960s' decade [10–12]. CDI is an electrosorption method in which a low electrical potential (0.6-2.0 V DC) is applied between two porous electrodes, in order to remove ions from a solution by adsorbing them onto the electrical double layers (EDLs) formed on the surface of the electrodes [1,17]. This technique is gaining popularity because of its relatively low energy consumption (0.5-1.5 kWh m^{-3}), cost effectiveness and ease of maintenance [11]. CDI has received increasing relevance for various applications such as desalination, water purification, heavy metal removal and water softening [14]. Among the electrodes used in this technology, carbon materials have been regarded as the best option, since many of them are derived from sustainable biomass, and so, the synthesis costs are usually very low and possess the unique ability to realize high surface area [18]. The carbon materials that jump out as the most interesting are activated carbons (ACs), carbon aerogels, ordered mesoporous carbons (OMCs), carbon nanotubes (CNTs) and graphene [19].

Throughout this thesis, the carbon form in which we will focus on is a graphene based material. Graphene is one of the most popular topics for the past several years, especially after its discovery had warranted it with the Nobel Prize in Physics in 2010. This material shows unique electrical, mechanical, thermal and optical properties [20]. Furthermore, graphene-based materials have been intensively studied in the field of electrochemical energy storage, showing great promise for CDI applications due to their high intrinsic electrical conductivity as well as high surface area, both essential parameters to obtain high energy and power density electrodes [20,21]. At the moment, chemical vapor deposition (CVD) is considered as the most promising method to obtain high quality graphene in large scales, but has the disadvantages of being very time consuming as well as expensive [20]. In addition, current synthesis methods of porous graphene require high temperature processing, or multi-stepped chemical synthesis, diminishing their commercial potential. For this reason, the development of a straightforward synthesis of graphene-based materials is still a technological important goal [22].

In certain polymers, the graphenization of carbon atoms can be obtained by laser writing due to the easy absorption of long-wavelength radiation, which promotes photo-thermal effects. At the surface of the polyimide, this process allows the formation of a nanostructured and porous carbon network known as laser-induced graphene (LIG) [23]. This method is regarded as an easy and scalable approach to produce 3D porous graphene structures through a one-step laser scribing process from commercial polyimide films, which shows great potential to be used in applications such as electrode materials for interdigitated supercapacitors. Furthermore, this procedure shows great versatility, since the irradiation of the polyimide (usually with a CO_2 infrared laser) can be conducted under ambient conditions or in controlled atmospheres, conferring different qualities to the resulting LIG material [24].

This thesis resulted from a collaboration between the University of Aveiro and *Bosch Thermotechnology Aveiro S.A.*. Throughout this work, a procedure to obtain a porous LIG electrode is proposed, using a CO_2 infrared laser with a wavelength of 10.6 μm, irradiating on a Kapton film. The different combinations of the synthesis' parameters are studied through its morphological, structural and electrical characterization, with the purpose to apply the obtained porous LIG electrode in a CDI prototype designed by *Bosch*. The results of the LIG being applied to CDI are presented and discussed accordingly.

The present dissertation is composed of six chapters, being that the first one corresponds to its introduction, were the goals of the work are presented. Afterwards, the thematic of capacitive deionization is tackled, in chapter two, where it is presented the theory of this phenomenon as well as a state of the art review. Similarly, chapter three focuses on laser induced graphene. On the following chapter, all the characterization techniques used along this work are briefly described. Throughout chapter five the experiments performed are presented, as well as their procedures, namely regarding the LIG's production and characterization, and the tests performed with a CDI prototype, designed by *Bosch* for testing purposes, while using the LIG developed as the electrode. On the sixth chapter, the results regarding the experiments described on chapter five are presented, as well as their analysis. Finally, in the last chapter the main conclusions are discussed, along with some proposals of future work.

2. Capacitive Deionization (CDI)

2.1 Theoretical basis

Capacitive deionization is an exciting water treatment technology in which an electrical potential is applied between two porous electrodes, propelling the cations and anions in the aqueous solution that flows through them to be electrostatically adsorbed and stored inside the surface's pores, where the electrical double-layers are formed. The adsorption depends on several aspects, such as the applied potential, the solution's salt concentration, and the electrodes characteristics, like their conductivity, specific surface area and pore size [4,9,25]. In order to comprehend and predict the amount of salt that can be removed as function of the applied electrical potential is crucial to understand the concept of electrical double layer (EDL). Throughout the following section, it is discussed in detail the notion of EDL.

2.1.1 Electrical Double Layer

Electrical double layer is a basic, yet important concept in electrochemistry. Whenever an electrode is subjected to an electrical potential and put in contact with an ion rich solution, the interface between both mediums is occupied with counterions, because of the Coulomb force, forming the EDL [19]. Once the charge is no longer being applied, hence removing the Coulomb force, the electrode releases the ions previously held by it into the solution once again [9,26]. This process is used in CDI, as a deionization and regeneration process operation, respectively (Fig. 1). The first model for CDI on which EDL was taken into consideration was developed by Johnson and Newman in the 1970s [27].

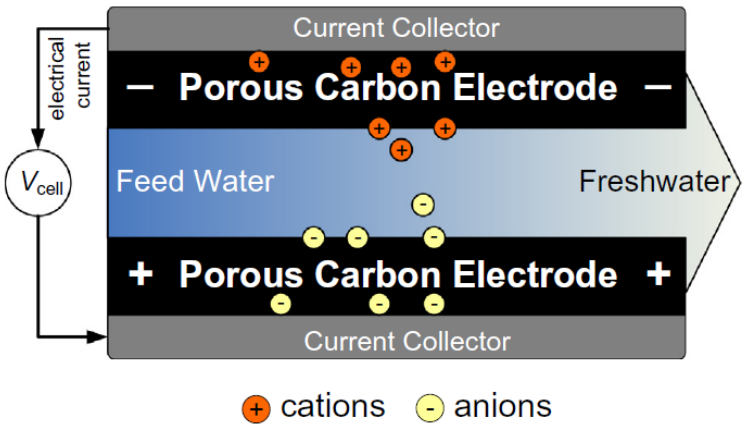

Figure 1: Scheme of the capacitive deionization cell, during the charge stage [4].

In the case of CDI, it is important to consider and analyse the interactions between the solution and the electrodes. Interfacial properties and structures between an electronic conductor and an aqueous electrolyte solution have been well described by the widely accepted Gouy-Chapman-Stern double layer theory [28]. According to this model, the double layer can be considered to be divided into two regions: the one closest to the electrode, named the Stern layer; and the Gouy-Chapman

layer, also known as the diffusion layer, where the distribution of the electric charge is dependent on the potential applied on the surface of the electrode [29]. The capacities concerning both of these layers contribute to the total capacitance. Hence, the total capacitance can be calculated as a series of both the Stern layer and the diffuse layer (Fig. 2). Therefore, the electrical capacitance of the interface, C_T, can be calculated with the following expression:

$$\frac{1}{C_T} = \frac{1}{C_S} + \frac{1}{C_D} \tag{2.1}$$

where C_S is the capacitance of the Stern layer, and C_D is the capacitance of the diffuse layer [19].

In a classic parallel-plate capacitor, the charge separation is electrostatic. Stern layer capacitance depends of the area of the plates as well as the separation between them, as shown in equation (2.2):

$$C_S = \varepsilon_r \varepsilon_0 \frac{A}{D} \tag{2.2}$$

where A is the area of each plate (m^2); ε_r is the relative permittivity of the material between the plates (also known as dielectric constant); ε_0 is the permittivity of free space with a value of $8{,}854\times10^{-12}$ F/m; and D is the separation between the plates (m).

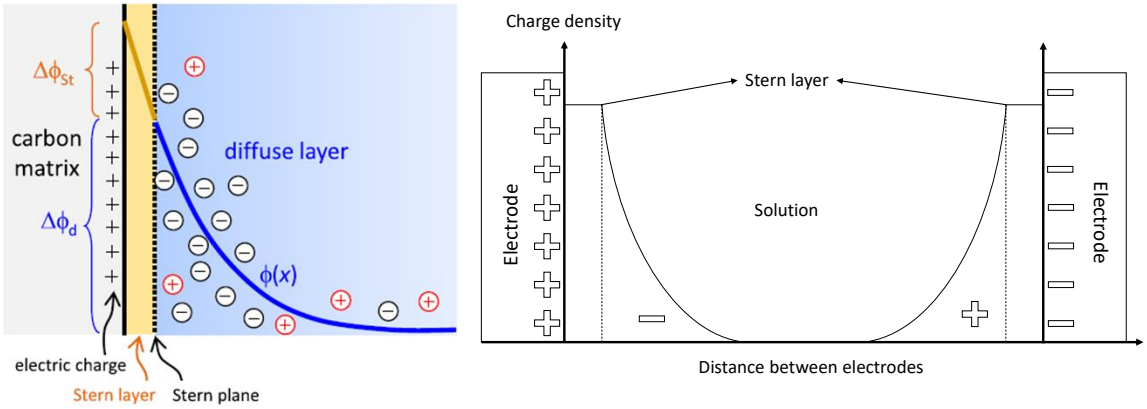

Figure 2: Illustration of the charge distribution in the Gouy-Chapman-Stern model (left) [4] and a scheme of the charge distribution in a two electrode system (right), image adapted from [15].

However, the capacitance of the diffusion region of the double layer cannot be calculated using the same expression of the inner one. To solve this issue, Gouy and Chapman developed an expression which shows the dependence of the charge excess, q , in mol/m^2, with the potential at the Stern plane, $\Delta\Phi_d$ (Eq. 2.3), considering the ions as punctual charges, assuming an ideally polarized electrode (no electron transfer through the interface) and ignoring the ion adsorption associated with other interactions [4],[19].

$$q = 4\lambda_D c_{salt} sinh\left(\frac{1}{2}\Delta\Phi_d\right) \tag{2.3}$$

where c_{salt} is the salt concentration, λ_D is the Debye length, given by $\lambda_D = 1/\kappa$, with the inverse Debye length being given by:

$$\kappa = \left(\frac{2F^2 c_{salt}}{\varepsilon_0 \varepsilon_r RT}\right)^{1/2} \tag{2.4}$$

with R being the universal gas constant, T the absolute temperature and F the Faraday constant. In order to obtain q in C/m^2 we have to multiply it by F. So, combining equations (2.3) and (2.4) we can write:

$$q = (8\varepsilon_0\varepsilon_r RTc_{salt})^{1/2} sinh\left(\frac{1}{2}\Delta\Phi_d\right) \quad (2.5)$$

Furthermore, differentiating the charge with respect to the potential at the Stern plane one obtains the capacitance of the diffuse layer:

$$C_D = (4\varepsilon_0\varepsilon_r RTc_{salt})^{1/2} cosh\left(\frac{1}{2}\Delta\Phi_d\right) \quad (2.6)$$

Even though both C_S and C_D contribute to the total capacitance of the double layer, in practical CDI processes, C_S is much more prevalent for ion capacitance. According to the expression (2.2), in standard capacitors, high capacitance values can be achieved by decreasing the distance, by using dielectric materials with very high permittivity, as well as using electrode materials with high surface area. In the particular case of EDL capacitors, the distance D is extremely small, corresponding to the thickness of the Stern layer, in the order of a few nanometres. This allows for a huge increase on the capacitance value. Hence, the focus turns into the development of electrodes with high specific surface area to obtain maximum capacitance [19].

When it comes to the calculation of the salt concentration at position x (distance from the Stern layer), two different approaches can be used to determine it [4]. On one hand, if the pore size (radius) is much larger than the Debye length, the Gouy-Chapman-Stern can still be used, being written as it follows:

$$c_j(x) = c_{salt} e^{-z_j\phi(x)} \quad (2.7)$$

where z_j is the ionic charge number (ion valence) and $\phi(x)$ is the dimensionless potential relative to that in the neutral bulk solution, and corresponds to the voltage V divided by the thermal voltage V_T. On the other hand, if the pore size is smaller than the Debye length, the EDLs overlap strongly, which makes the Gouy-Chapmen-Stern model no longer applicable. When this happens, the approach used is the Modified Donnan theory [30,31], which includes a chemical attraction energy for the ion when it transfers from outside to inside the carbon particles, which is represented by the term μ_{att}. Knowing that, the salt concentration according to the modified Donnan theory is [32]:

$$c_j(x) = c_{salt} e^{-z_j\phi(x)+\mu_{att}} \quad (2.8)$$

Nowadays, the Modified Donnan theory is regarded as the most reliable approach to explain the CDI phenomenon.

2.1.2 CDI systems performance metrics

Throughout most CDI papers, salt concentration reduction of the feed stream during a CDI cycle is the most reported metric. However, it has become clear that this metric does not provide sufficient insight about the electrodes or the cell performance, since the salt concentration reduction can be affected by a great variety of parameters (for instance, feed velocity) [31]. For this reason, it is crucial to consider additional metrics to describe the performance of CDI systems.

A growing trend in CDI is to measure the salt adsorption capacity (SAC) of a cell's charge and discharge cycle, a metric first introduced by Soffer and Folman [33]. The CDI cycle can have any duration, from very short to very long. When the equilibrium is reached the maximum salt adsorption capacity (mSAC) is measured, occurring when the measured conductivity of the cell's effluent no longer varies over time. Both mSAC and SAC are given by the following expression:

$$SAC = \frac{m_{salt}}{m_{elec}} \quad (2.9)$$

where m_{salt} (mg) is the mass of salt removed from the feed water and m_{elec} (g) is the mass of both of the electrodes while dry.

However, the SAC gives no information on the rate at which the salt adsorption occurs. Hence, the average salt adsorption rate (ASAR) is introduced as a very important metric do describe CDI performance. This measurement has been reported in units of $\mathrm{mg\,g^{-1}min^{-1}}$, being the SAC over time. The time period usually considered is how long it takes for a charge and discharge cycle to be completed. While the SAC is a metric specific of the electrode, ASAR describes the full system, and depends on the cell's structure as well as on the electrode's material [31].

Furthermore, another metric of interest in the characterization of a CDI system is the charge efficiency, Λ, and is given by the following expression:

$$\Lambda = \frac{\Gamma_{salt}}{\Sigma} \tag{2.10}$$

where Γ_{salt} is the amount of removed salt upon applying a cell voltage and Σ is the total charge accumulated in the electrode pair during charging (divided by Faraday's number) [4]. The charge efficiency is an equilibrium property, requiring enough time for the desalination to come to an end, and is a function of the applied cell voltage during charging and discharging, as well as the feed water concentration. This metric is always less than unity. For the duration of the CDI cycle, the cations and anions of solution will be stored in the pores of the cathode and anode, respectively. However, before the cell voltage is applied, some may have already been brought into the pores (Fig. 3a), and once the cell voltage is applied, several phenomena can happen, namely: some of these ions will be expelled from the pores due to having the same charge, the co-ion expulsion (Fig. 3b), which lowers the Λ value since ions are released to the solution; the counterions are adsorbed into the pores, the counterion adsorption (Fig. 3c), which increases the Λ, balancing the previous phenomenon; no change on the solution concentration occurs during the charging step, the ion swapping (Fig. 3d), causing the Λ to remain constant [31,34,35]. This parameter is crucial when determining the energy requirements of a CDI system, and usually, higher values of Λ lead to lower energy consumption [4,31]. Related to the previous metric, the ratio between the ASAR ($\mathrm{mol\,s^{-1}}$) and current (A) divided by the Faraday's constant is known as the current efficiency, λ.

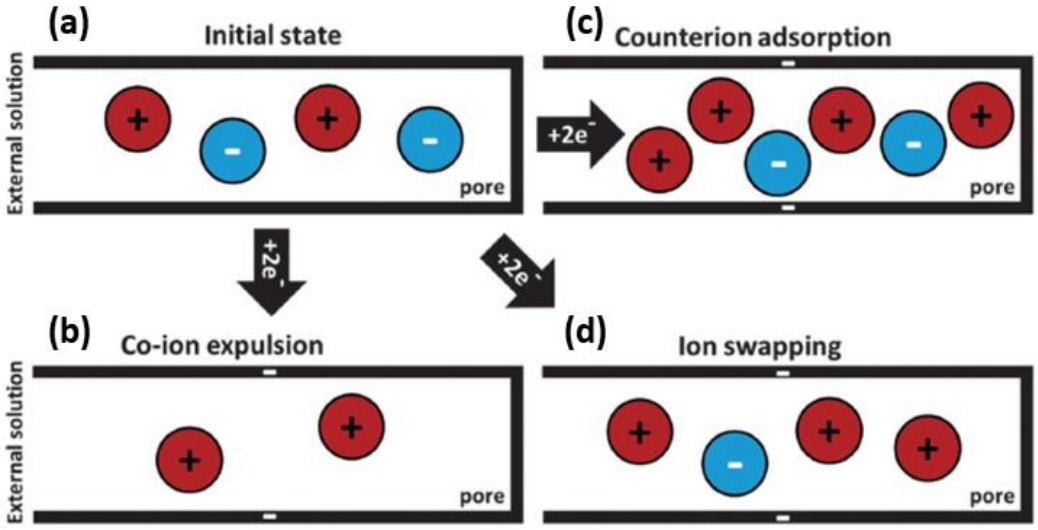

Figure 3: Illustration of the fundamental electric charge compensation mechanisms with increasing cell voltage from the (a) initial state to the (b) co-ion expulsion, (c) counterion adsorption and (d) ion swapping [31].

Furthermore, in order to know the salt's concentration, the water's conductivity is measured. These two parameters are related to each other according to the following expression [36]:

$$C_w = \frac{F^2}{RT}\sum_i z_i D_i c_i \tag{2.11}$$

where z_i, D_i and c_i are the valence coefficient, diffusion coefficient and salt concentration, respectively, of the salt i, and C_w is the water's conductivity. However, the desalination tests are usually carried out with a one salt solution, and the concentration and quantity of the salt is known *a priori*. Thus, the equation that is used to characterize the desalination process focuses solely on the percentage of salt removed from the solution, as it is shown in equation (2.12):

$$SR(\%) = \frac{C - C_0}{C} \times 100 \tag{2.12}$$

in which SR is the salt removed, C is the initial water conductivity and C_0 is the final conductivity [37].

2.2 CDI systems

Throughout the past decade, the field of CDI has been object of a great number of innovations and exponential growth, which propelled the development of different operation geometries and modes, as well as new electrode materials. These areas of CDI are addressed in this section.

2.2.1 CDI vs MCDI

One of the most promising developments in CDI is the incorporation of ion-exchange membranes (IEMs) in front of the electrodes (Fig. 4), a technology called Membrane Capacitive Deionization (MCDI). IEMs have a high internal charge, therefore allowing easy access for one type of ions (counterions) and blocking the passage of opposite charged ones (co-ions). This feature improves the charge efficiency values of the desalination system. With an additional modification, IEMs can also be made to have selectivity between ions with the same charge sign (like nitrate and chloride ions) [4,38].

Furthermore, MCDI also has the advantage of being able to operate at reversed voltages during ion release, which is no possible in conventional CDI. Once the voltage is reversed, both electrodes are depleted of the counterions previously adsorbed, but these are not adsorbed again on the opposite electrode due to the presence of the IEMs. This provides a great clean-up of the electrode's structure, which propels for the increasing of the counterion adsorption rate and capacity compared to CDI [39]. However, this technology has the disadvantages of the additional cost arising from the addition of the membranes, as well as their short lifetime.

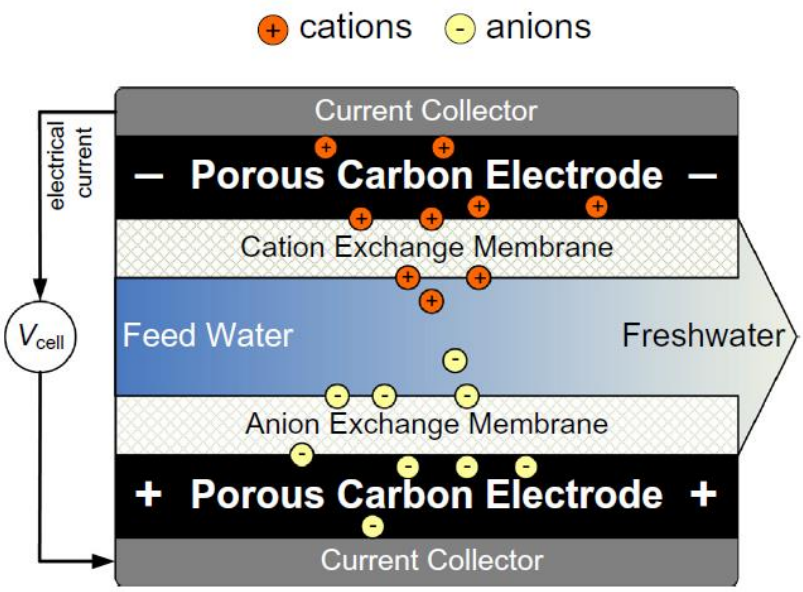

Figure 4: Illustration of a membrane capacitive deionization cell during the charging cycle [4].

2.2.2 CDI geometries

Currently, several CDI cell's geometries have been explored, the most predominant ones being: flow-by mode, flow-through mode, electrostatic ion pumping and desalination with wires (Fig. 5). The first one, "flow-by" mode (Fig. 5a), is the type of geometry on which most of the CDI studies focus on. In this case, the set consists of two oppositely faced electrodes, separated by a thin gap through which the water flows. This design is the classical CDI geometry, and can be operated with a single cell pair or with a stack of multiple pairs. The space between the electrodes can be an open channel, usually with at least 1 mm thickness, or can be occupied by a spacer material (isolator), a porous thin layer with thicknesses that vary from 100 to 300 µm (reduced spacer thickness should lead to lower cell ionic resistance, as well as faster deionization by reducing the diffusion timescale for salt removal between the electrodes [4]). When using this design, several flow patterns arise (for example, in square electrodes): the water can flow from one edge of a square channel to an exit point at the opposite corner [40]; or it can flow from a hole in the centre of a square electrode radially leaving the cell on all four sides [41].

On the other hand, an arrangement can be conceived in which the water flows through the electrodes, the "flow- through" mode (Fig. 5b). In this approach, the feed water is pumped perpendicular to the electrodes, flowing through the larger pores of its structure. The direct migration of the ions into the electrodes enhances the rate of desalination, when compared to the "flow-by" mode [4].

Another design used in CDI systems is called "electrostatic ion-pumping" [42] (Fig. 5c), that offers the possibility of having two separate outward streams: a fresh and a concentrated water streams at opposite ends of the device. The feed water is pumped into the system from the top side, and a cell voltage is applied in an on/off faction, in order to have the charge and discharge of the electrodes. At the on state, two valves open on opposite ends, allowing the feed and freshwater to leave the cell separately. At the off state, the valve through where the freshwater was previously leaving closes, since at this moment there is no desalination [4].

Finally, the CDI geometry illustrated in Fig 5d is the “desalination with wires” method [43]. The biggest advantage of this approach is the fact that the feed and freshwater streams are separated right from the beginning. The operation occurs within two steps: first, an array of anode and cathode wires is submerged into a water stream, while an electrical tension is applied; second, when the wires have reached their maximum salt adsorption, the array is placed on another stream, and the voltage set to zero so that the ions previously adsorbed are released. This two-step process is repeated the amount of times it is required to obtain a freshwater stream.

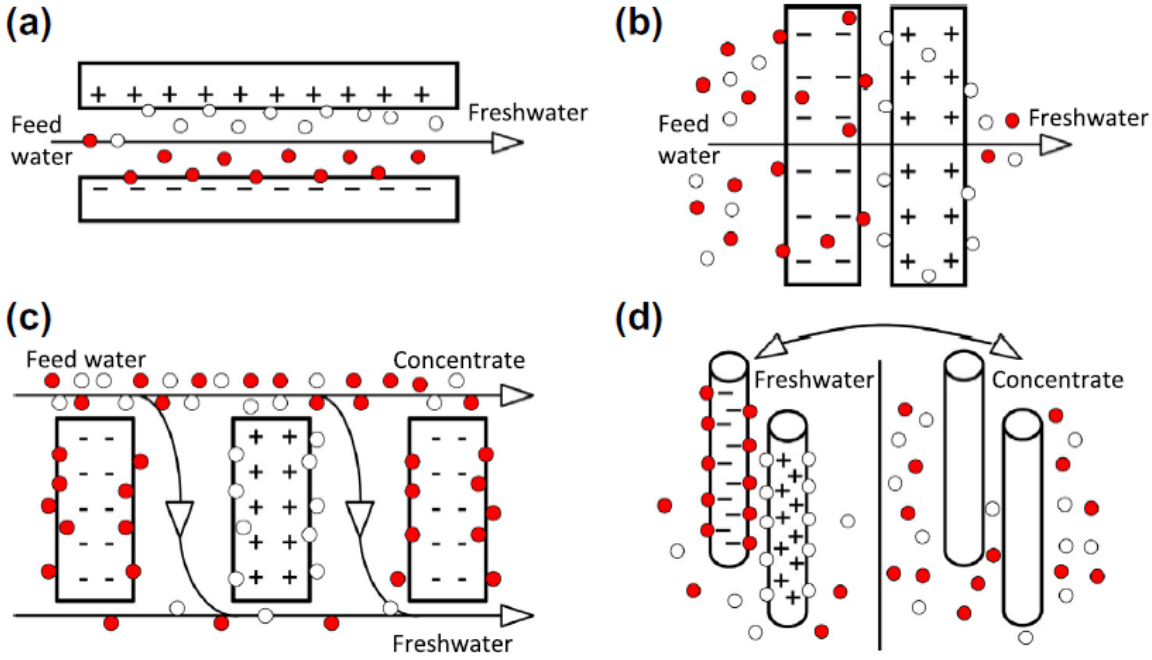

Figure 5: Illustration of the most relevant CDI geometries: (a) flow-by mode, (b) flow-through mode, (c) electrostatic ion pumping and (d) desalination with wires [4].

In this thesis, the flow-by mode was chosen due to its simplicity and easiness of implementation.

2.2.3 Constant current (CC) vs constant voltage (CV) modes

Almost every CDI work that has been published reports on procedures where a constant voltage operation (CV-operation) is used [4]. With this method, a constant cell voltage is applied, promoting the ion adsorption. The ion concentration in the effluent is reduced abruptly as the voltage stars to be applied, and then starts to increase again towards the initial value, meaning the system has reached its deionization capacity (Fig. 6). Once the voltage is no longer applied (or reversed), the ion desorption occurs, resulting in the salt release and the system’s regeneration. Usually, in CDI applications, the values of the cell voltages are low, since the water’s electrolysis starts to occur at 1.23V. For this reason, most of the published work uses voltages of 1.2V, in order to prevent the previous phenomenon from happening, while using the highest voltage possible.

However, due to the way the salt’s concentration varies throughout the desalination cycle (Fig. 6), the CV-operation is not the most practical mode for freshwater generation. When generating freshwater, it is important that the outward water maintains a constant salt concentration, which

cannot be obtain with the CV-operation. This can be achieved maintaining a constant current (CC-operation) instead of the voltage. This way, the outward's salt concentration remains fairly constant, at a low value during the adsorption step and high during the desorption one. Furthermore, this operation mode also has the advantage of providing the possibility to accurately tune the effluent salt concentration level by adjusting the electrical current or the water flow rate [4,44].

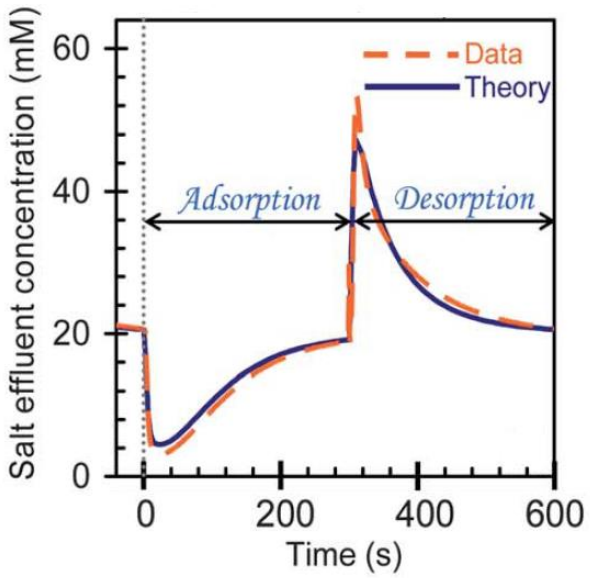

Figure 6: Variation of the salt effluent concentration throughout a (M)CDI in a CV-operation [44].

Unfortunately, the constant value during de adsorption can only be achieved using MCDI (Fig. 7). This is due to the fact that in CDI the electrical current is partially compensated by counterion adsorption and co-ion desorption (reason why MCDI shows a higher charge efficiency than conventional CDI). The co-ion desorption effect decreases at high voltages, where the current is proportional to the water desalination rate. However, this does not happen at low voltages, causing for the effluent salinity in CDI-CC to not stabilize at a constant value. Once the CC-operation is applied in MCDI, the constant levels of the salt concentration are quickly reached, since the co-ions are trapped within the electrodes, due to the IEMs [4,44].

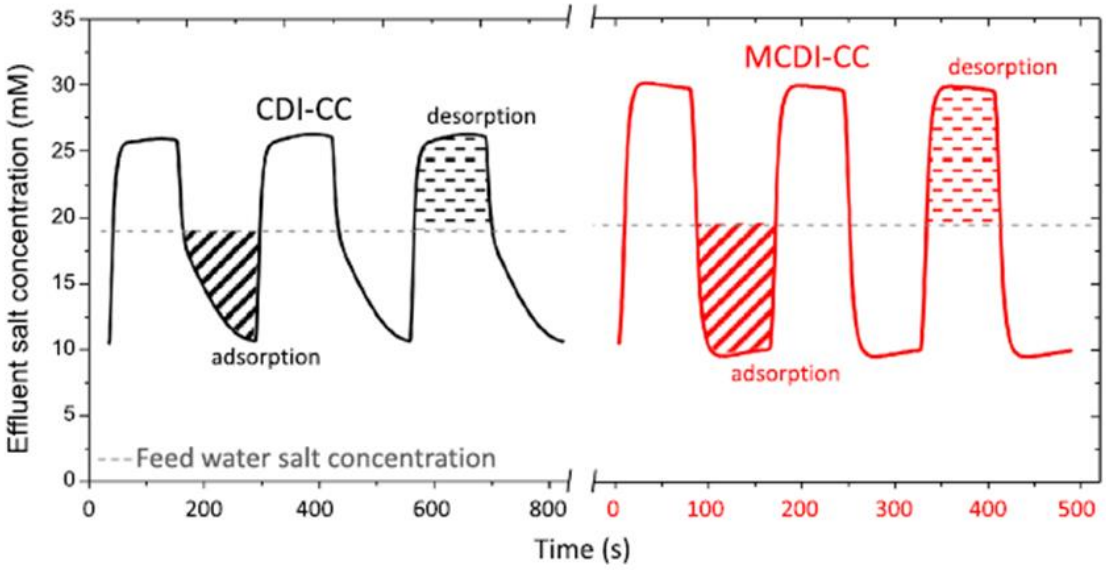

Figure 7: Comparison between the CC-operation in CDI and MCDI [4].

2.2.4 Single-pass vs Batch-mode experiments

Regardless of the CDI geometry used, the crucial aspect is the CDI desalination capacity. This is accomplished by measuring the change of the salt concentration over time, either by analyzing water samples' composition (in the case where there are several different salts in the water) or, by simply measuring the water conductivity (single salt solution).

The measurement of the outward feed's conductivity can be done with two different methods: single-pass (SP-method) and batch-mode (BM-method) [4]. In the first case [39], the water is fed from a reservoir directly to the CDI system, and the conductivity probe is placed at the exit of that container. Afterwards, two things can happen, either the water leaving the CDI system is discarded or it can be sent back to the reservoir, and in either one of them, the conductivity is also measured at the cell's exit. Concerning the latter option, the reservoir needs to be large enough so that the overall salt concentration of the water in it does not vary significantly. In this method, once the cell voltage is applied, the salt concentration shows a very sudden drop, followed by a steady rise to the inlet value, due to the fact that the electrodes have reached their maximum salt adsorption capacity (Figure 8a).

In the BM-method [37], the water reservoir is much smaller, and the water's conductivity is well controlled and measured inside the tank. In this case, the water that exists the CDI cell flows back to the reservoir (Figure 8b), thus the salt concentration drops steadily until its minimum value.

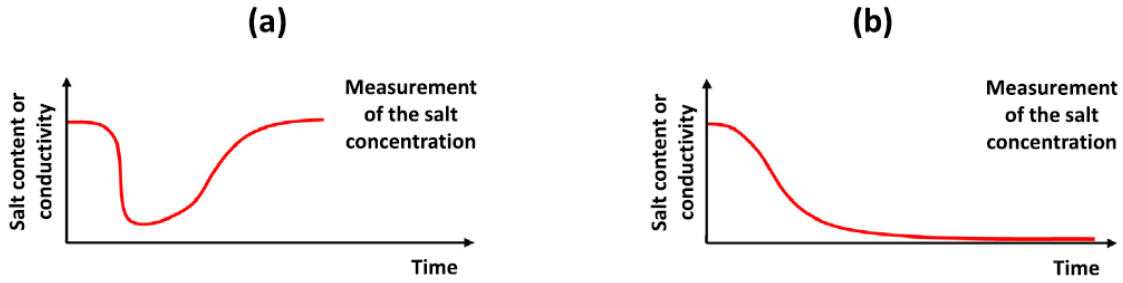

Figure 8: Variation of the conductivity over time for the (a) SP-method and (b) BM-method [4].

Even though, the BM-method appears to be the simpler method, it is not the most rigorous one. The concern arrives from the difficulties in comparing results from different experiments, since the salt concentration is measured at a different initial value in each experiment. For instance, in the BM-method is very difficult to compare data for equilibrium adsorption at the same salt concentration for a range of voltages, since different voltages result in different desalination rates, thus different salt concentrations. This problem does not appear in the SP-method, since all properties can be measured at well-defined values of the feed stream. In addition, the SP-method also has the advantage of being the one most reminiscent of a CDI application, where the water only passes through the system once. For these reason, along the experiences regarding the CDI prototype, the SP-method will be the set up used.

2.2.5 Electrode materials

The electrodes are a very critical component in CDI, since are responsible for the adsorption and storage of the ions. As it was mentioned previously, porous materials are regarded as the best option for water desalination applications. However, the materials' porosity is not the only requirement to be taken into consideration. In the following list, it is highlighted the most important characteristics of an adequate CDI electrode [15,45]:

- High specific surface area (SSA);
- High electronic conductivity;
- Fast ion mobility within the pore network;
- Low contact resistance between the porous electrode and the current collector;
- Easily shaped according to design requirements;
- Low economical cost;
- High bio-inertness;
- Good wettability.

Furthermore, because of pore's importance in the desalination process, it is worth to clarify the nomenclature used. While the International Union of Pure and Applied Chemistry (IUPAC) has defined pores merely in their size (Table 2) [15], this terminology does not account for the difference between materials, especially when these materials have complex pore structure. For this reason, some CDI authors distinguish micropore from macropore in a different way, as it is illustrated in Fig. 9:

Table 2: Pores classification according to the IUPAC.

Type of pore	*Size*
Macropores	>50nm
Mesopores	2-50 nm
Micropores	<2 nm

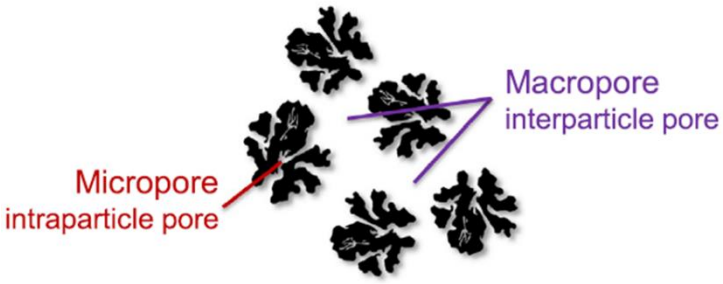

Figure 9: Pore classification in CDI [4].

In order to obtain maximum performance, the pores should be large enough so that only weak EDL-overlap, which means that mesopores are preferred to micropores. However, in some carbon materials such as activated carbons [46] and carbide-derived carbons [47], micropores show better results compared to the mesopores. Thus, porous electrodes that combine a large micropore volume with a network of mesopores and macropores may show better results in the deionization process [48].

From the vast range of materials that can be used as CDI electrodes, the carbon-based are the ones most used and studied, due to having very high SSA, good electrical conductivity and chemical/physical stability. In addition, carbons are very easily processed and cheap. In Table 3, it is presented some of the most used type of carbon for CDI applications:

Table 3: Values of the specific surface area for different carbon materials.

Carbon material	SSA (m^2g^{-1})	Reference
Activated Carbons	730-2195	[49]
Carbon Aerogels	400-1100	[50]
Ordered Mesoporous Carbons	950-1594	[51]
Carbon Nanotubes	49-129	[52]
Graphene	222	[53]
Carbon Blacks	<120	[54]

Nowadays, activated carbons are the most used carbon materials, not only due to their superior SSA but also for their low cost and for being derived from natural sources such as coconut shells, wood, coal or synthetic sources like resins [4]. However, the use of graphene in CDI applications has gain interest in the recent times, as it has been proved to have both higher salt adsorption capacity and faster ion immobilization rates when compared to other carbon materials [55,56]. Thus, as mentioned in the Introduction section, this was the selected material for the present work, where a simple laser processing technique was employed in the growth of the LIG electrodes.

3. Laser Induced Graphene (LIG)

Like it was previously mentioned, graphene has been intensively studied due to its exciting potential, especially in the area of electronics, but a simpler way to obtain graphene is still a work in progress, particularly for large-scale production. As a mean to overcome this challenge, the method of laser scribing has surfaced. In this technique a laser beam, typically from an infrared (IR) laser, is pointed into a polyimide (PI), material like Kapton films, promoting the growth of 3D-graphene layers over it [22]. The resulting material is designed as laser-induced graphene (LIG) and a schematic representation of the process is illustrated in Fig. 10.

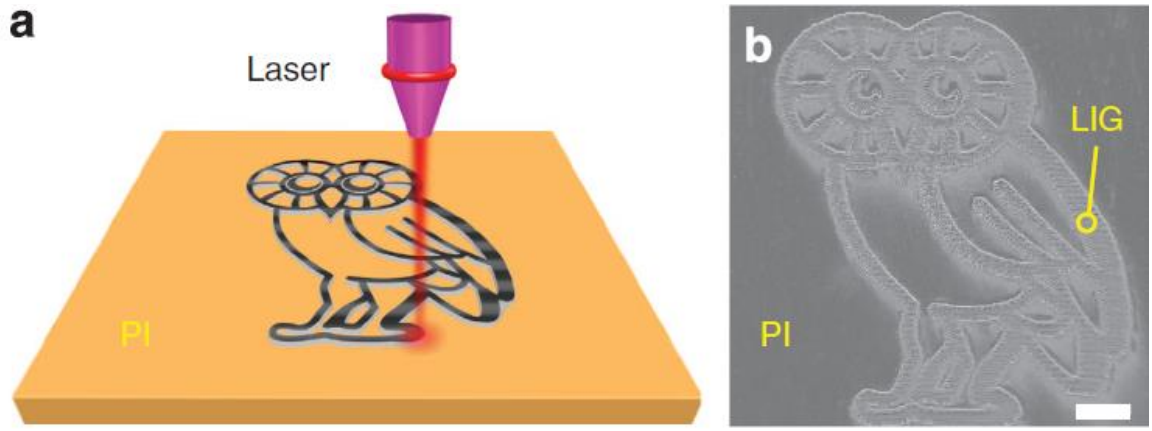

Figure 10: (a) Schematic representation of the LIG synthesis process from PI; (b) SEM image of LIG patterned into an owl shape. Scale bar 1mm [22].

In certain polymers, the graphenization of carbon structure occurs through photothermal effects (thermal bond breaking by light), which can be obtained by laser writing. In the LIG process, the laser's energy induces lattice vibrations by locally increasing the temperature, causing the sp^3-carbon atoms to be photothermally converted into sp^2-carbon atoms. The latter can recombine or be released as gases, originating the porous graphene structure. This graphene layout shows superior power and energy density once applied in energy storage devices like electrodes for microsupercapacitors (MSCs) [21,22,24].

In this thesis, the polymer used is polyimide (commercially known as Kapton), which has the ability to maintain its physical, electrical and mechanical properties along a vast range of temperatures (from -269°C up to 400°C), as well as chemical stability [57]. Furthermore, its flexibility is also an interesting asset for LIG applications.

In 2014, Jiam and colleagues [22] introduced a one-step scalable approach for producing and patterning porous graphene films from commercial polymers using a CO_2 infrared laser. The resulting LIG showed high electrical conductivity, and a great potential towards its use in MSCs, having specific capacitances >4 $mF.cm^{-2}$ and power densities of ~9 $mW.cm^{-2}$. This propelled for various studies regarding this type of LIG applications, like its combination with other pseudocapacitive materials, such as manganese dioxide (MnO_2) and iron oxyhydroxide (FeOOH) [58], and molybdenum disulfide (MoS_2) [59]. Furthermore, a study regarding the LIG synthesis has been conducted by Andrea Lamberti and colleagues [23], and have shown that scan speed (80-200 mm/s, with increments of 40 mm/s) and pulse frequency (4-24 kHz, with increments of 4 kHz) of the incident radiation induced different structure rearrangements and conduction properties.

While most of the LIGs are grown in ambient conditions (exposed to air), they can be produced in different atmospheres, which can promote the emergence and/or improving of its properties. For example, using selected gas atmospheres, a major change in the water contact angle on the LIG surface can be obtained, from 0° (superhydrophilic) when using O_2 or air, to over 150° (superhydrophobic) with Ar or H_2[24]. Furthermore, another area where LIG has proven to be very useful is the life sciences. For instance, the authors of reference [60] developed LIG layers and electrodes to be used in biofouling prevention (all instances of fouling where biologically organisms are concerned [61]). It was shown that the produced material was extremely biofouling resistant, and once used as an electrode exhibited exceptional antibacterial properties. Once voltages were applied (1.1-2.5 V) to the electrodes, a rapid bacterial movement occurred towards the LIG, and subsequent killing of these microorganisms (Fig. 11 - left).

Additionally, LIG can be used to *give voice to the voiceless*, or with some sort of speech impediment. Lu-Qi Tao and colleagues [62] presented an intelligent artificial throat, capable of not only generating sound, but also detecting it (Fig. 11 - right), based on LIG, with high efficiency, high flexibility and low cost. This technology relies on the thermoacoustic effect to generate sound, and on the porous morphology of LIG to detect sound. In order to generate sound, a low voltage is applied to the device, and the Joule heat causes the air expansion, resulting in sound waves. On the other hand, the vibration of the throat cords will cause a change in the device's resistance, varying its current, which enables the sound detection. This equipment offers the possibility of turning meaningless sounds, like a cough or a scream, to manageable and predesigned sounds.

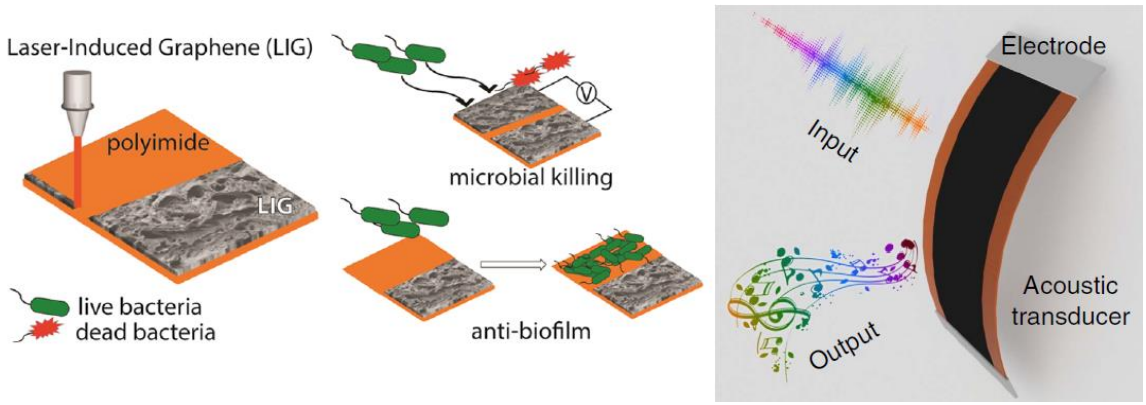

Figure 11: Illustration of the bacteria interaction with the LIG [60] (left) and the ability if emitting and detecting sound in one device [62] (right).

4. Characterization techniques

4.1 Raman Spectroscopy

Vibrational spectroscopy has shown to be an important contributor in several fields of science, ranging from physics, to engineering, chemistry and biology. Furthermore, Raman measurements provide the vibrational spectrum of the analyte in a non-destructive manner, which can be seen as the "fingerprint" of the studied material, since it can provide information about the structure, symmetry, electronic environment and bonding of the molecules [63,64].

Raman spectroscopy is based on the light-matter interaction. Whenever a photon of energy $h\upsilon$ reaches a material, three types of scattering can occur: Rayleigh, Stokes and anti-Stokes (Fig. 12). Firstly, in the Rayleigh scattering, the material is excited to a higher virtual energy state, but rapidly decays to the initial vibrational energy state, emitting a photon with the same energy. Secondly, in Stokes scattering, the interaction between the incident photon and the material causes the molecule to gain energy, which causes the frequency of the scattered light to be lower than the incident one, with energy $h\upsilon - E_v$. This is caused by a decay to a higher vibrational energy state than the initial one. Finally, in the anti-Stokes scattering, the emitted photon has an energy of $h\upsilon + E_v$. This means that the material decays to a lower vibrational energy state than the initial state, which means that the starting state is not the fundamental one. This type of transitions has a lower probability of happening, which explains why they exhibit lower intensity peaks on the Raman spectrum [64].

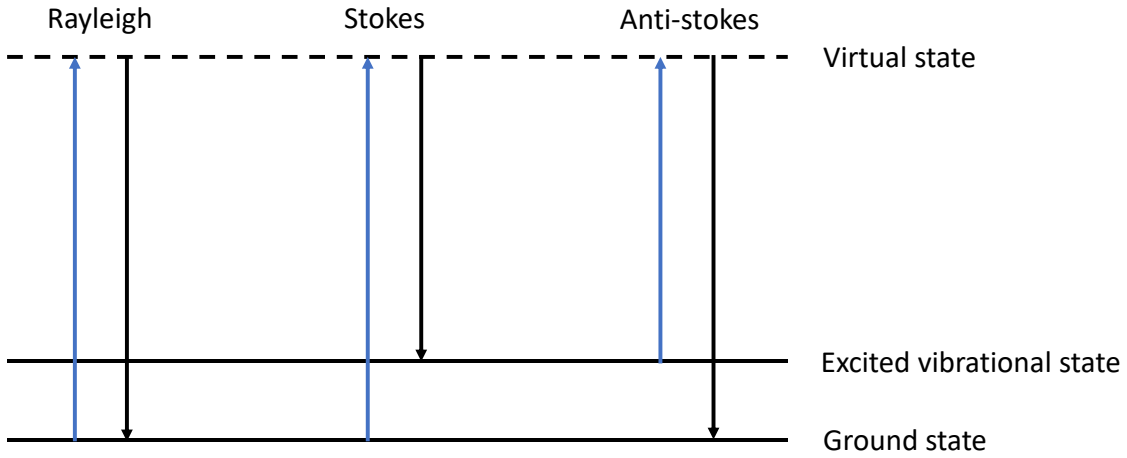

Figure 12: Energy level diagram of the states involved in Raman spectroscopy, image adapted from [64].

This technique has become one of the most popular in the characterization of disordered and amorphous carbon, fullerenes, nanotubes, diamonds, carbon chains and polyconjugated molecules. Accordingly, Raman techniques are especially useful for characterizing graphene due to the absence of band-gap, which makes all wavelengths resonant, hence the Raman spectrum contains information about both atomic structure and electronic properties [65]. For these reasons, Raman spectroscopy was used throughout this thesis to study and evaluate the quality of the LIG produced.

4.2 Scanning Electron Microscopy (SEM)

SEM is a well-established method and one of the most interesting and effective in the characterization of the surface and morphology of materials at micro and nanoscales (Figure 13 - right). Nowadays, SEM is a widely used tool in various fields such as materials and surface sciences, semiconductor research and life sciences, among others. In SEM, the electron beam is emitted from the cathode and accelerated into the sample with a voltage ranging from 0.1-30 kV. The interaction between the electron beam and the sample results on the scattering of secondary electrons (among other types) and X-rays (Figure 13 - left). These are the two most relevant scattering components. With the mapping of the secondary electrons' intensity it is provided crucial information about the sample's surface morphology. On the other hand, the X-rays can be used in Energy-dispersive X-ray spectroscopy (EDS), which gives the elemental identification in the sample [66].

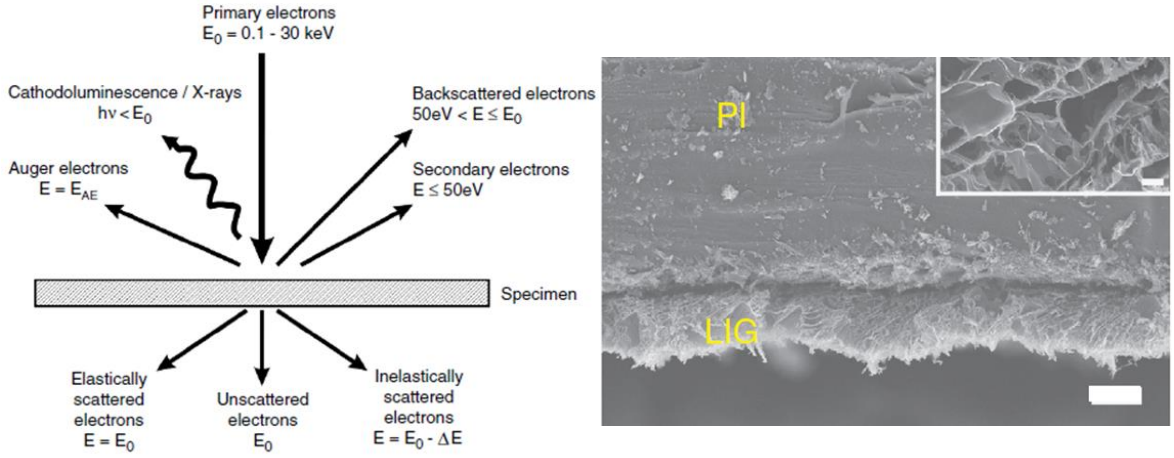

Figure 13: (left) Schematic drawing of signals for a thin sample generated by the impinging electrons in SEM. E_0, energy of beam electrons; E, energy of signal electrons; E_{AE}, energy of Auger electrons; ΔE, energy loss of inelastically scattered electrons; $h\nu$, radiation's energy [66]. (right) cross-sectional SEM image of the LIG film on a PI substrate, scale bar 20 µm. Inset is a SEM image that shows the porosity of the LIG, scale bar 1 µm [22].

4.3 Van der Pauw measurements

In order to evaluate the quality of the LIG produced for electrode use, the sheet resistance was assessed, R_{sheet}, which is a measure of resistance of thin films with uniform thickness. The sheet resistance is expressed in ohms per square ($\Omega/\square$) so it is not confused with the conventional resistance [67].

Throughout this thesis, the Van der Pauw method was used to measure the sheet resistance of the produced LIGs. In this method, four contacts are positioned at the boundaries of the sample. In the present case, the contacts were placed at the vertices since the samples were squared (Figure 14). Firstly, a current I_{12} is supplied through the contacts 1 and 2, and the voltage drop V_{34} is measured across the contacts 3 and 4. Afterwards, the same procedure is applied to calculate the resistance in the other direction, by feeding a current I_{14} and measuring the voltage drop V_{32}. Both the resistances are calculated with the following expressions:

$$R_{hori} = \frac{V_{34}}{I_{12}} \tag{4.1}$$

$$R_{vert} = \frac{V_{32}}{I_{14}} \tag{4.2}$$

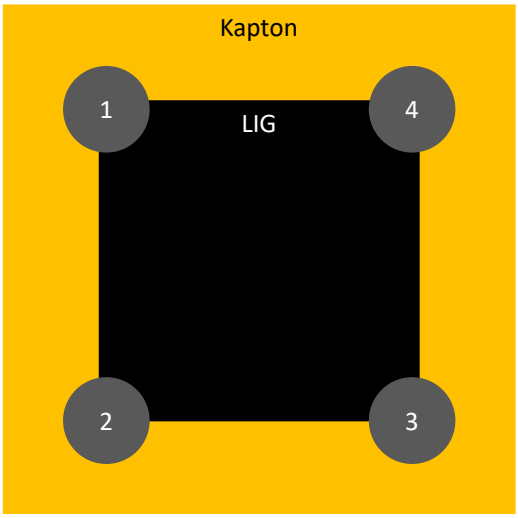

Figure 14: Scheme of the experimental apparatus used to measure the LIG's R_{sheet}.

Following the current and voltage measurements, the R_{sheet} was determined, using a numerical method, with the following expression [67]:

$$R_{sheet} = \frac{\pi R_{vert}}{ln\left(1 + exp\left(-\frac{\pi}{R_{sheet}}(R_{vert} - R_{hori})\right)\right)} \tag{4.3}$$

4.4 Water flow stability tests

The LIG was developed with the intent to be used as electrodes in a CDI cell prototype, which means that the material had to show stability when in contact with a water flow. Having said that, an experiment was idealized where a LIG sample was subjected to a constant water flow (tap water), and its mass and sheet resistance were measured, as well as SEM imaging. This characterization was performed before and after the exposure to water. In this way, it was possible to verify the stability of the LIG samples, when exposed to a water flow of 6 l/min.

In order to perform these experiments, the equipment shown in Fig. 15 was constructed, which consists in a plastic cylinder, with water entries/exits at the bottom and top of it, and a sample holder inside the cylinder. This sample holder was placed in a way that the water passing through the apparatus would pass along the sample, instead of perpendicular to it (emulating the flow-by mode). Once one of the entries was connected to a water tap, the structure would be filled before allowing the water to leave on the opposite end. Once the container was full, the water can leave the structure. This procedure guarantees that the water flow is constant along the sample, and prevents the emergence of gases in the liquid.

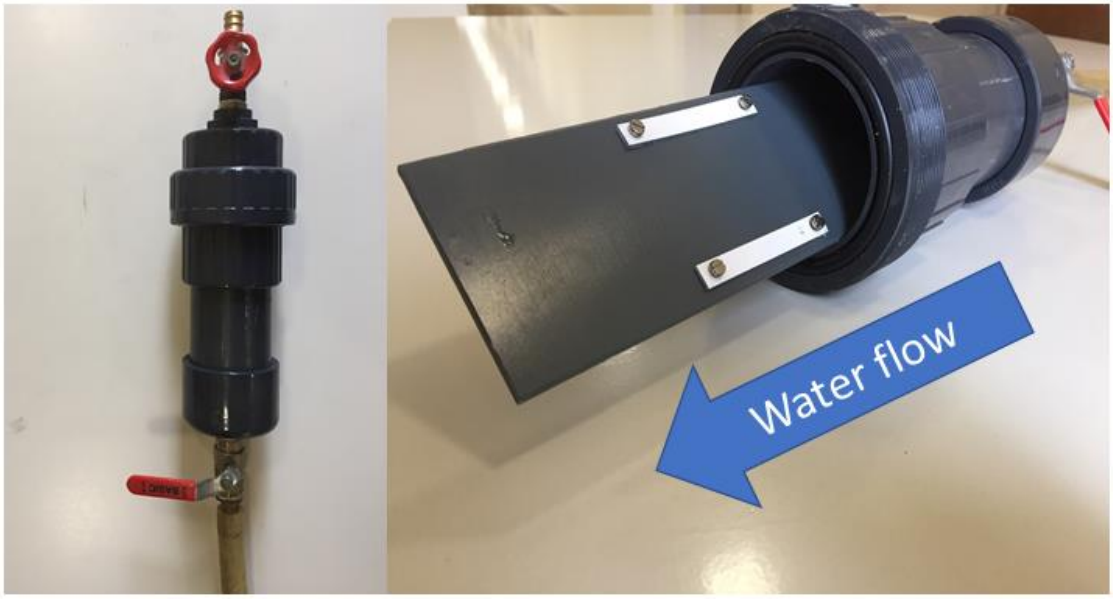

Figure 15: (left) Set up used for the LIG water stability tests; (right) sample holder.

4.5 Brunauer Emmett Teller (BET) method

Brunnauer *et al.* [68] have developed the most used method of determination of solids' specific surface area and pore size, the BET method. This method, relies on the adsorption of chemically inert gases, such as nitrogen, argon or krypton, to measure the entire surface area of a sample, including the one contained in micropores and mesopores [69,70]. The equipment used for BET measurements calculates the specific surface area through the determination of the quantity of gas adsorbed in the sample's surface. These measurements are performed at the gas condensation temperature, so that the adsorption occurs. The gas is pumped into the container were the sample is placed (in vacuum) from another one where the gas is stored at a known pressure P^0. Afterwards, the pressure on the sample's container, P, is measured. After some time, the equilibrium is reached (when the pressure in both the gas and sample containers is the same), the sample is retrieved and the volume of gas adsorbed n is measured [71]. This procedure is repeated for different values of P^0, and the specific surface area is calculated performing a linear regression of the following expression [72]:

$$\frac{1}{n\left(\frac{P^0}{P}-1\right)} = \frac{c-1}{n_m c}\left(\frac{P}{P^0}\right) + \frac{1}{n_m c} \tag{4.4}$$

where P/P^0 is the relative pressure, n_m is the BET monolayer capacity and c is the BET constant. Usually, the data is plotted as $1/\left(n(P^0/P-1)\right)$ against P/P^0, and n_m and c are calculated from the slope and interception of the resulting regression line. To obtain the BET surface area, the monolayer capacity is often divided by a predetermined monolayer density, ρ_m, which is often quoted in literature describing porous absorbents and substrates [72].

4.6 Characterization equipment

The Raman studies were conducted in the backscattering configuration on a Jobin Yvon HR800 instrument (Horiba, Japan), with a 600 lines/mm grating and a laser line of 442 nm, resulting of a HeCd laser (Kimmon Japan). The objective used was one of 50×, to focus the laser light onto the samples, as well as to collect the backscattered Raman radiation for later detection by the Peltier cooled (223 K) CCD sensor. Furthermore, the spectrometer was used in the confocal mode, with the iris set to 300 μm. SEM imaging was carried away with a TESCAN VEGA3 in secondary electron imaging mode and the Van der Pauw measurements were conducted with a precision source/measure unit (SMU) KEYSIGHT B2902A, in the four-wire mode. Finally, BET analysis was done with a Gemini V2380 from *Micrometrics Instrument Corporation*. The degassing was performed at 100 ºC overnight with a hydrogen flux.

5. Experimental procedures

5.1 LIG production

As it was previously mentioned, a continuous CO_2 laser with a wavelength of 10.6 µm and a maximum power output of 50 W was used to produce the LIG samples. The procedure followed to create each sample is illustrated in Fig. 16. From here, we can highlight three laser parameters: scan speed v(mm/s); distance between laser lines d(mm); and the laser power output (%P_{max}). The used equipment does not provide a discrete value of power, P, which is why these values where measured with a power meter, in order to attribute definite values to this parameter.

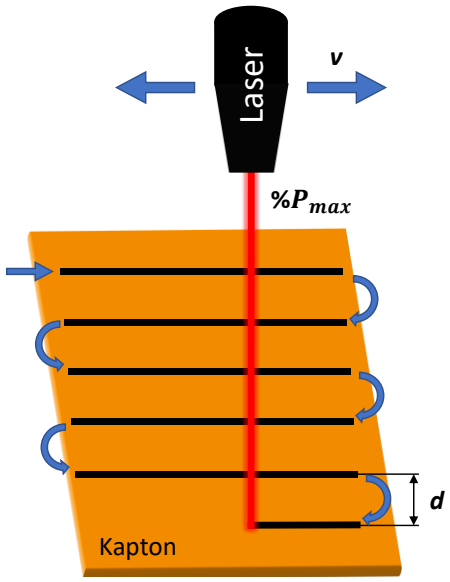

Figure 16: Scheme of the procedure used to obtain LIG samples.

These three parameters were the ones found to be the most influential on the LIG production process, reason why different combinations of them were studied in order to optimize the desired material properties. The scan speed was varied from 100-500 mm/s, whereas the power output went from 10-50 %P_{max}. The distance between lines' influence was studied for the values of 0.03, 0.075, 0.1 and 0.125 mm.

The samples produced were always squares. The ones which were to be studied via Raman spectroscopy and SEM were 5×5 mm^2 in size, while the remaining samples where always 40×40 mm^2. Furthermore, the distance between the laser and the Kapton was always equal to the focal distance, which was 18 mm. Furthermore, while the laser was irradiating on the Kapton, it was crucial that the film remained as flat as possible, so that the distance between it and the laser did not vary. To ensure it, the polyimide was placed over a metal plate and fixed with small magnets.

5.2 CDI tests

5.2.1 Electrode preparation

On the CDI prototype designed by *Bosch*, it was required that the electrode was conductive from the back to the front of it, so that the current collector could be attached at the back of the electrode (as in the case of the *Siontech* module showed in subsection 6.2.1). In the case of the LIG, this is not possible, since Kapton is an insulator. For these reason, a modification was done so that our material could be applied in the CDI module.

To solve this issue, holes were drilled in the Kapton film, with a diameter of 0.1mm, spaced 0.40 mm from each other's centres, as depicted in Fig. 17 - left. To do so, a pulsed ultraviolet (UV) laser with a wavelength of 355 nm was used. Afterwards, LIG was grown on both sides of the Kapton film, in a way that all of the LIG's area would overlap the holes. This allowed it to be able to flow current from one face to the other, since both LIG faces are now connected with the Kapton film. This is possible because, upon exposing the Kapton film to the laser radiation, the beam is able to reach the holes' walls, which promotes the LIG's growth there. This is evidenced in the cross-section SEM image depicted in Fig. 17 – right, which shows the presence of LIG through all the sample's thickness.

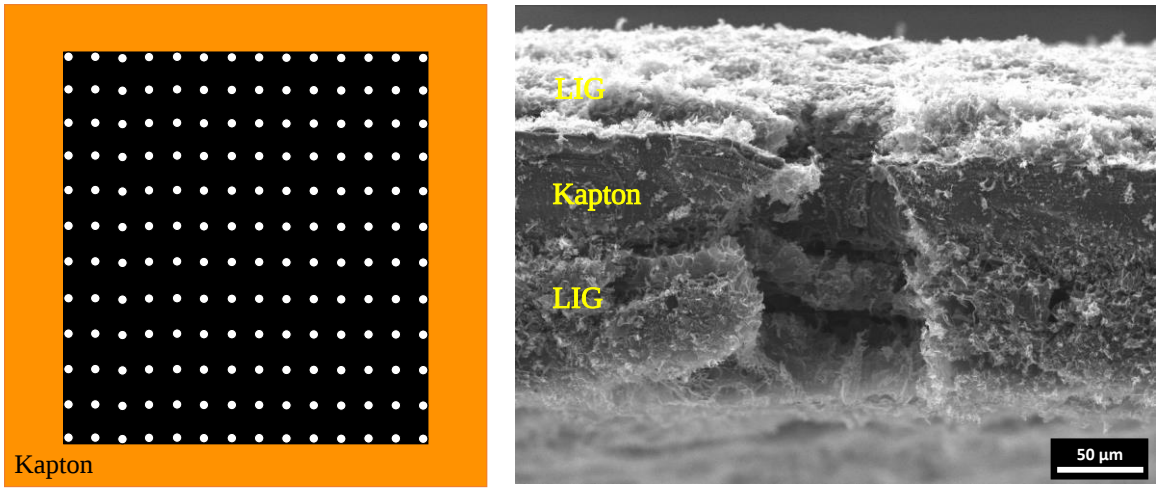

Figure 17: (left) Scheme of a perforated LIG sample processed by UV laser; (right) cross-section of a sample where LIG was grown on both sides of perforated Kapton.

5.2.2 CDI testing apparatus

In order to assess the capabilities of the developed LIG concerning its CDI application, two different experimental apparatus where conceived. Firstly, two LIG electrodes, prepared as it is depicted in the previous subsection, were applied in the prototype designed and constructed by *Bosch* for our tests. The set up used was the one shown in Fig. 18, where a bottle was placed at 1.85 m above the ground, and hoses were used to transport the water throughout the whole system. Between the bottle and the CDI module (#3 in Fig. 18 - left), two tap-like components were used, one so that the water flow could be controlled and fixed (#1 in Fig. 18 - left), and another to be used as an on/off "switch" (#2 in Fig. 18 - left). Throughout these experiences, the voltage applied on the CDI module was always of 1 V, with the use of a SMU.

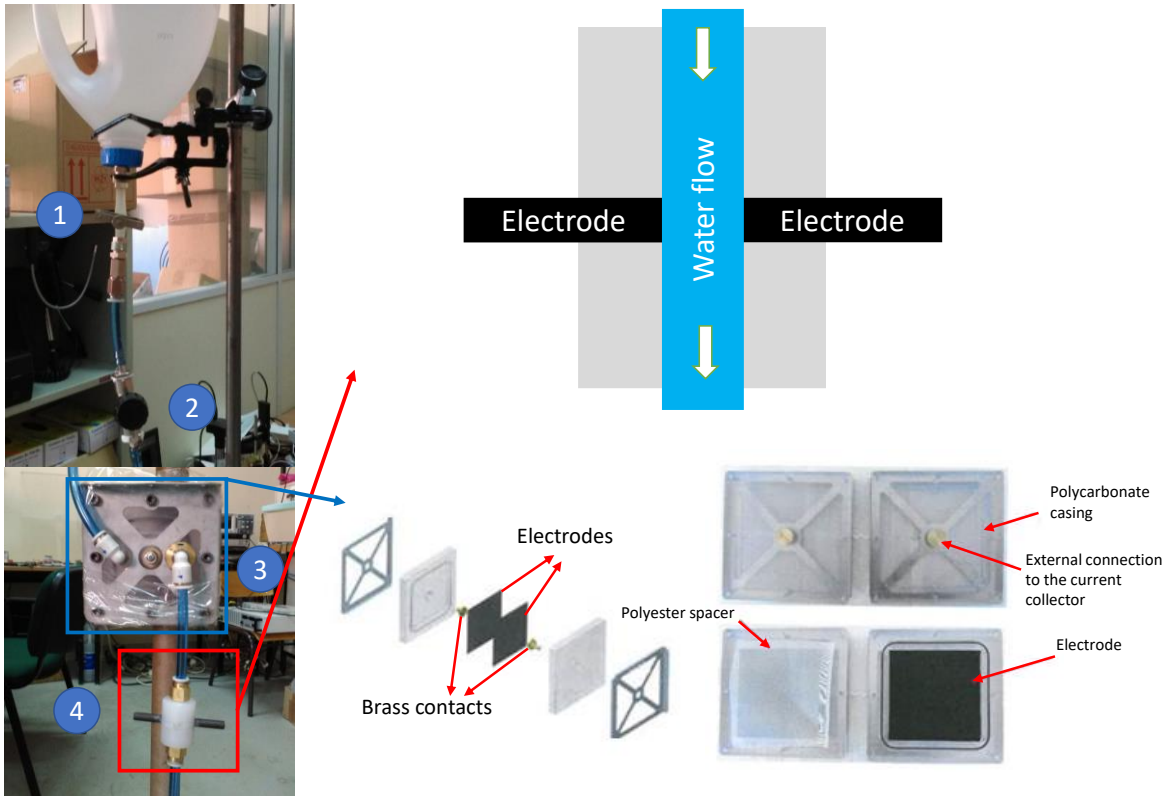

Figure 18: (left) Photographs of the CDI experiment apparatus used with the testing prototype and (right) a scheme of the conductivity measurement set up (top right) and the components composing the testing prototype (bottom right).

Furthermore, in order to measure the water's conductivity, an improvised set up was conceived (Fig. 19 - right), which consisted of two graphite electrodes and a nylon tube. The electrodes were placed at a fixed distance between each other of 10 mm (L), and where both cylindrical in shape, with a radius of 5 mm, which provides the area of the electrodes surface (A). This set up allowed to determine the conductivity using expression 5.1 [73], knowing the resistance between the electrodes (R). In order to determine R, it was used the circuit depicted in Fig. 19 - left, where a voltage source was used to apply an alternating voltage of 1V, so that the water electrolysis would be avoided [74]. Knowing the value of the voltage applied (V_{in} = 1 V), the value of the first resistance (R_1 = 266.7 Ω) and V_{out} (measured by the voltmeter), it is calculated the value of R (expression 5.2, voltage divider), needed to determine the water conductivity.

$$\sigma = \frac{L}{RA} \tag{5.1}$$

$$R = R_1 \frac{V_{out}}{V_{in} - V_{out}} \tag{5.2}$$

After the water passed through the conductivity meter, it was stored in a recipient.

Secondly, another CDI set up was idealized to measure the charge and discharge curves of the LIG and two other commercial electrodes. This time, the positive electrode would be placed facing the negative one, distanced 10 mm from each other. The area of electrode submerged in water was of 6.5×2 cm^2, and the water used had a concentration of 0.56 M of NaCl. The concentrated water used in the experiments resulted from adding NaCl to common bottled water (*Penacova*). In addition, to ensure that the electrodes did not bend, they were duct taped to microscope blades. For measurement purposes, the SMU was once again used, and a MATLAB GUI was used to record the potential difference and current variations over time. In this experiment, two different modes were

considered: the constant voltage mode (CV-mode) and the constant current mode (CC-mode). In the first one, it was applied a voltage of +1V between the electrodes, and once the current value had stabilized, the voltage was set to zero, and waited for the current to stabilize once again, obtaining this way the charge and discharge cycles. In the CC-mode, currents of 5 mA and -5 mA were supplied to the *Siontech*'s and *Kuraray*'s electrodes, and the voltage variation was measured. For the LIG, the current fed to the electrode was of 1 mA and -1 mA, so that the measurement could be done, since for higher currents, the system would saturate too fast for measurements to be made. In Fig. 19 - right is an illustration of the set up used for these second group of CDI experiments.

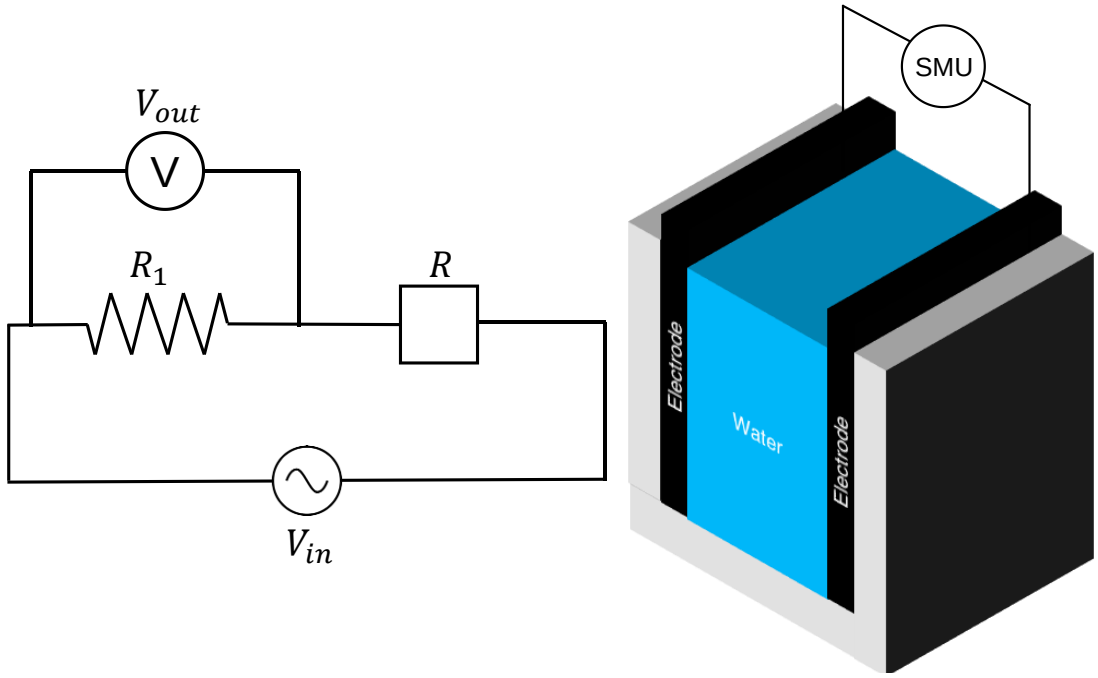

Figure 19: Illustration of the (left) circuit used on the conductivity measurements and (right) of the experimental set up used on the second group of CDI experiments.

6. Results and discussion

6.1 LIG's optimization and characterization

LIG samples were prepared by laser irradiation on Kapton film varying the scan speed of the laser beam between 100-500 mm/s and the laser power between 10-50 $\%P_{max}$, with increments of 100 mm/s and 5 $\%P_{max}$, respectively. The distance laser between lines remained constant across all the samples at the value of 0.05 mm. Initially, 5×5 mm^2 samples were produced for SEM imaging and Raman spectroscopy characterization. This allowed for an initial evaluation on the quality of the samples, regarding both its composition as well as surface morphology.

The Raman analysis showed the presence of Kapton on some of the samples, mainly for low values of both power and scan speed, which is not desired, since it diminishes the electrical conductivity of the resulting LIG. However, some configurations showed great quality LIG without the presence of Kapton (background in black spectrum of Fig. 20 - left), mainly at intermediate values of both power and scan speed. Furthermore, SEM imaging (Fig. 20 - right) provided great insight on the surface morphology of the samples. Namely, the emergence of fibres for high values of laser power, possibly due to the overlap of the laser scanning combined with high power values. These fibres were proven to deteriorate the electrical properties of the obtained LIG, since the resistances measured across (R_{vert}) and along (R_{hori}) the sample were very different, being the R_{vert} considerably higher. In addition, it was also possible to notice the presence of large amounts of small pores, which is a desired feature, since the material is to be used as an electrode in CDI, and ion storage is predicted to occur in the pores.

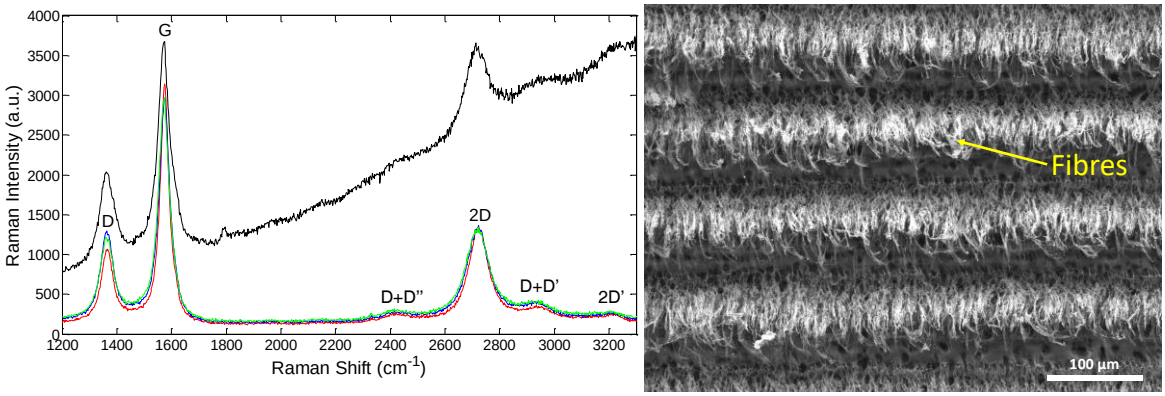

Figure 20: (left) Raman spectra in four different places of a sample produced with a scan speed of 300 mm/s, 15 $\%P_{max}$ and a distance between lines of 0.05 mm; (right) SEM image of the surface of a sample produced with a scan speed of 300 mm/s, 30 $\%P_{max}$ and a distance between lines of 0.05mm.

Throughout the characterization of this first set of samples, a correction on the alignment of the laser beam had to be performed. This caused a variation on the values of its power output (Table 4). However, it is important to notice that, despite this correction of the power values, the results obtained maintained the same dependence regarding the studied parameters, but for other laser power values. Thus, SEM and Raman spectroscopy had to be repeated for a new set of samples. On the following set of samples (Fig. 21), the power parameter was only studied in the interval from 15-25 $\%P_{max}$, since it was already understood that for higher power values the quantity of fibres that would

appear on the LIG was considerable, regardless of the scan speed, while at lower power outputs it was not possible to promote the material's growth. Additionally, this new set of samples was also created with a distance between lines of 0.1 mm, since it was the distance perceived to be the most adequate, as promoted the least laser overlap and the best sheet resistance values, while maintaining the best uniformity throughout the samples' surface.

Table 4: Variation of the laser power values before and after the laser alignment correction.

$\%P_{max}$	P_{before} (W)	P_{after} (W)
10	1.0	1.7
20	7.7	9.7
30	13.1	15.0
40	-	19.4
50	22.4	23.9
60	19.7	25.8
70	22.3	26.6
80	22.5	27.8
90	19.6	30.0
99	22.3	28.4

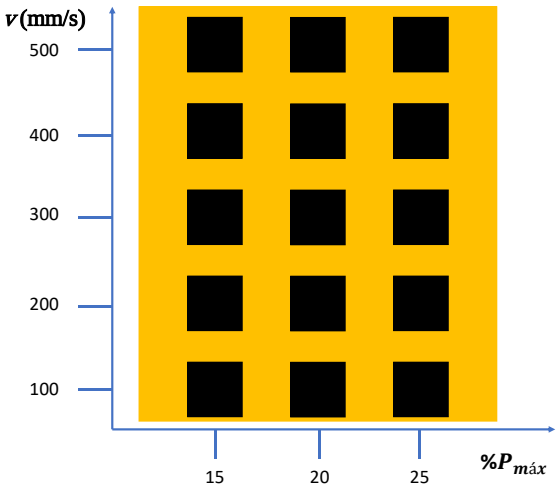

Figure 21: Scheme of the second set of LIG samples.

Raman spectroscopy was performed on all the samples schematized in Fig. 21, with the same purpose as before. This allowed to eliminate the samples obtained at speeds over 300 mm/s due to the presence of Kapton on the large majority of them.

Considering these results, only the samples produced at the scan speeds of 100, 200 and 300 mm/s where studied via SEM which showed, once again, that the appearance of fibres was higher for greater values of power, especially for values over 15 $\%P_{max}$. Furthermore, with the increase in scan speed, the uniformity of the sample was compromised, showing zones of great porosity alternated with zones with considerably less. Afterwards, the electrical characterization of the LIG samples was performed. This was done measuring the sheet resistance (as depicted in section 4.3) of the LIG samples, and the results showed a variation of the sheet resistance for the various combinations of parameters. In Table 5 are presented the values measured for this property, as well as the SEM images, for the samples produced with scan speeds under 300 mm/s.

Table 5: SEM images and sheet resistance values for the samples produced with scan speeds between 100-300 mm/s and for power values of 15-25 $\%P_{max}$.

300 mm/s	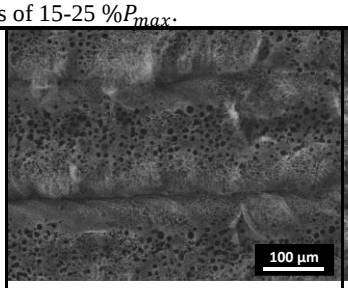	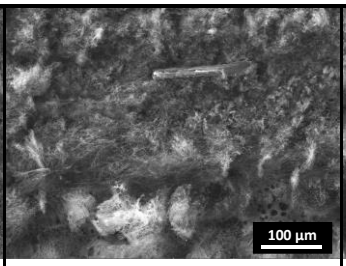	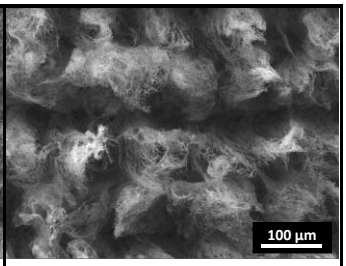
	$R_{sheet} = 111.44\ \Omega/\square$	$R_{sheet} = 138.75\ \Omega/\square$	$R_{sheet} = 530.93\ \Omega/\square$
200 mm/s	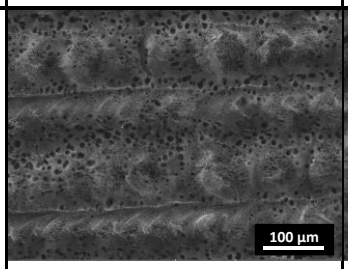	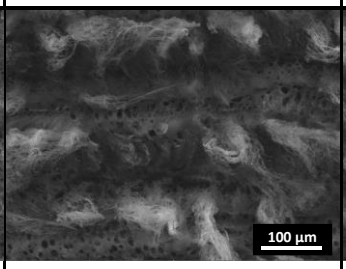	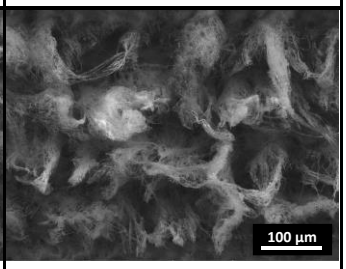
	$R_{sheet} = 40.31\ \Omega/\square$	$R_{sheet} = 70.13\ \Omega/\square$	$R_{sheet} = 64.72\ \Omega/\square$
100 mm/s	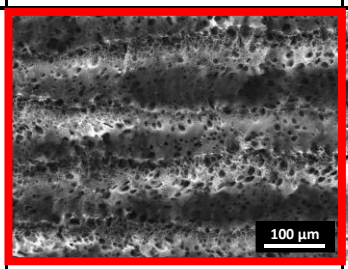	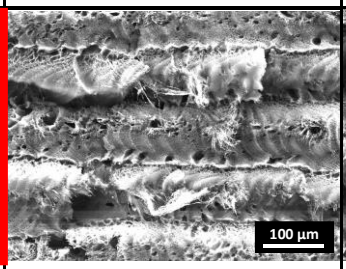	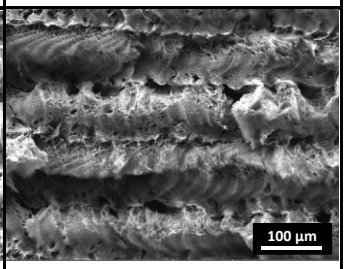
	$R_{sheet} = 34.25\ \Omega/\square$	$R_{sheet} = 71.21\ \Omega/\square$	$R_{sheet} = 83.34\ \Omega/\square$
	15 $\%P_{max}$	20 $\%P_{max}$	25 $\%P_{max}$

From these studies, it was possible to conclude that the configuration that showed the most potential was the one created at 100 mm/s and 15 $\%P_{max}$, since it was the sample that did not have fibres on the surface, while maintaining a great quality LIG, as well as surface uniformity. Moreover, it is also the one that exhibits the lowest value of sheet resistance.

The Raman spectrum presented in Fig. 22 offers great insight about the quality of the LIG obtained under these conditions. Firstly, at ~1369 cm^{-1} appears the D band, which suggests the existence of defects on the sample, since it does not appear in high quality graphene, and corresponds to the breathing modes of the sp^2 coordinated defective graphite phases [63,75]. Further along, at ~1578 cm^{-1} is the G peak, which results from the bond stretching of the sp^2 C-C bonds. In our LIG, the G peak is the one with the highest intensity, which points to a high number of graphene layers. However, the quotient between these two peaks is I_D/I_G~0.21, which indicated small size of the defects [65,76]. Furthermore, the third main peak that can be highlighted in the LIG spectrum is the 2D band at ~2730 cm^{-1}. In pure graphene, this band is the most intense, and is the D peak overtone, while the 2D' (~3222 cm^{-1}) is the D' overtone, which usually appears at ~1620 cm^{-1} . Both the D and 2D peaks appear on pure graphene because they originate from processes where there is momentum conservation, which allow it to satisfy the selection rules, while the D+D'', D+D' and 2D' bands are also typical of graphene-based materials [65]. In addition, the I_{2D}/I_G (0.32) points to the multi-layered of the graphene foams [76]. Finally, a noticeably smaller peak can be seen at ~2329

cm^{-1} (red circle), which corresponds to a nitrogen molecular vibration peak, present in the air nearby the laser focus region [77].

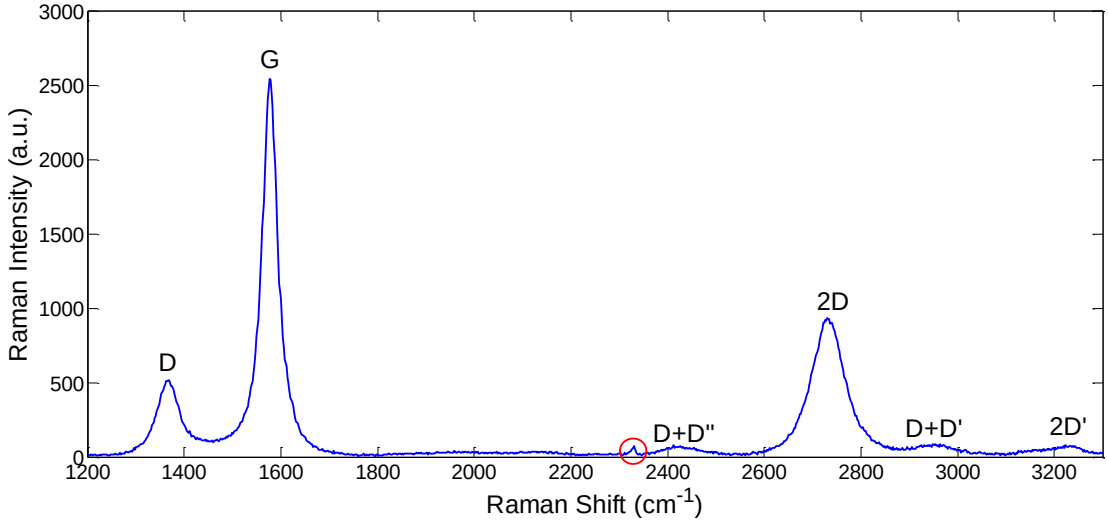

Figure 22: Raman spectrum of a sample produced at a scan speed of 100 mm/s, 15 $\%P_{max}$ and 0.1 mm of distance between lines

Even though the LIG spectrum cannot be identified as pristine graphene, considering the application to which is proposed to and the production technique, the resulting material is more suitable, interesting and promising. In fact, the Raman spectrum obtained is very similar to the one depicted in reference [22] (Fig. 23 - left), being the only noticeable difference the intensity of the 2D peak. This could show that our LIG has a more defective structure [65]. However, compared to LIGs described in other papers [59,60], our material shows not only a higher 2D band, but also a smaller I_D/I_G quotient, pointing to the good quality of our LIG (Fig. 23 - right).

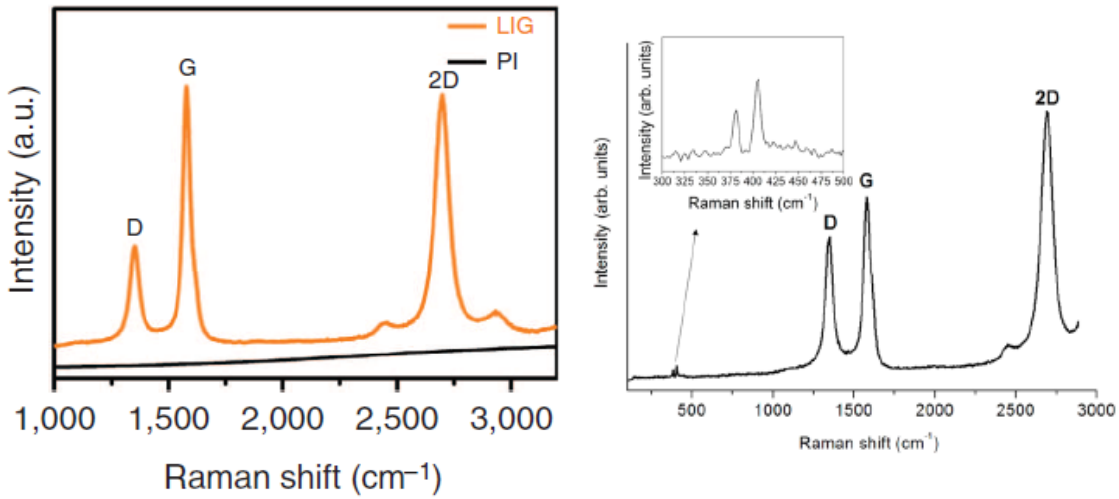

Figure 23: Raman spectra obtained in ref. [22] (left) and ref. [59] (right).

Considering the desired application, it is crucial to investigate if the produced material remained stable once it was subjected to a constant water flow, which was evaluated using the procedure explained in subsection 4.4. In order to perform the characterization aforementioned, four identical square LIG samples of 40×40 mm^2 were produced. These dimensions were chosen since it will be

the ones required to apply the LIG electrodes in the testing prototype. The samples were produced at a scan speed of 100 mm/s, 15 $\%P_{max}$ and 0.1 mm of distance between lines. The mass (Kapton plus LIG) and sheet resistance where both measured before and after being subjected to a constant water flow. In addition, Raman spectroscopy was also performed before and after the LIG being in contact with water. The results of these experiments are presented in Table 6 and Fig. 24.

Table 6: Values measured for the sheet resistance and mass for four LIGs produced with the same laser parameters and size, but subjected to a constant water flow for different periods of time.

	R_{sheet} (±0.02 Ω/□)		m (±0.001 g)	
	Before	After	Before	After
LIG1 (0 min)	32.02	29.42	0.661	0.664
LIG2 (3 min)	36.09	31.31	0.660	0.663
LIG3 (5 min)	35.88	32.99	0.672	0.675
LIG4 (10 min)	38.81	34.54	0.664	0.667

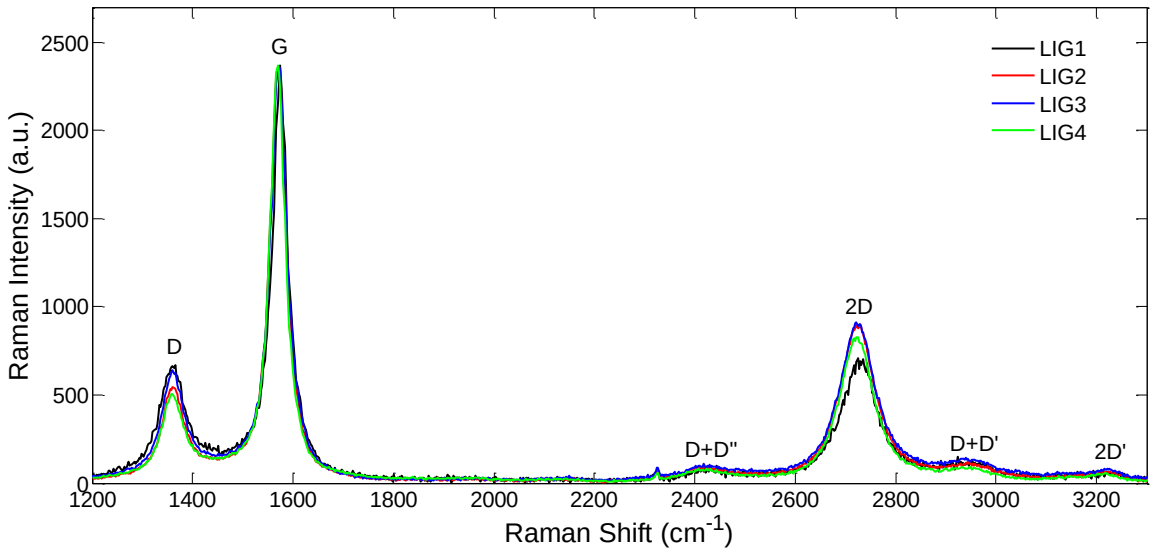

Figure 24: Raman spectra of the four LIGs produced samples with the same synthesis parameters and size, but subjected to a constant water flow for different periods of time.

From these results, several conclusions can be drawn about the quality and stability of the LIG samples. Firstly, looking at the mass variation on the samples, it can be seen an average increase of ~0.003 g on every sample. Even though it is not a substancial variation, it is worth pointing that, regardless of the duration of time that the LIG is subjected to a constant water flow, or whether it is subjected to it or not, the variation is approximately constant. This can indicate that the LIG samples produced have a great specific surface area, since their weight increase suggests that some water and/or air could have been stored in the pores, even though the samples were placed in an oven at ~70°C for 20 min, approximately twenty-four hours after performing the water stability tests. Secondly, the sheet resistance showed a decrease between the measurements made before and after the water tests. However, these differences are not significant, since the variation of both R_{hori} and R_{vert} are very small (Table 7). On the other hand, this could point to the removal of some fibres or other components that lower the electrical properties. This effect can be seen in the SEM images in

Fig. 25, where a sample of LIG produced under conditions favourable for a great amount of fibres (scan speed of 500 mm/s, 25 $\%P_{max}$ and 0.1 mm of distance between lines) was exposed to a constant water flow, where it can be seen that these components were almost completely removed. Finally, Raman spectroscopy proved the stability of the LIG's throughout the water tests, not showing any significant modifications on its structure. Additionally, the specific surface area obtained for the LIG produced with this configuration (scan speed of 100 mm/s, 15 $\%P_{max}$ and 0.1 mm of distance between lines) was of 148.36 m^2/g and an average pore size of 4.91 nm. Jian Lin and colleagues [22], obtained a LIG with a surface area of ~342 m^2/g. Despite having a bigger surface area compared to ours, the pores sizes are very similar, presenting different pore sizes from 2.36 nm to 8.9 nm. Yet, the discrepancy between the surface area values might arise from the difference of laser power used, being our LIG obtained with a power of 4.38 W, while in the article it was used a power of 3.6 W.

Table 7: Values measured of R_{hori} and R_{vert} for four LIGs produced with the same laser parameters and size, but subjected to a constant water flow for different periods of time.

	R_{hori} (±0.01 Ω/□)		R_{vert} (±0.01 Ω/□)	
	Before	After	Before	After
LIG1 (0 min)	3.67	3.99	5.98	5.68
LIG2 (3 min)	3.73	4.18	6.61	6.03
LIG3 (5 min)	3.84	4.17	6.61	6.28
LIG4 (10 min)	3.52	3.94	6.89	6.44

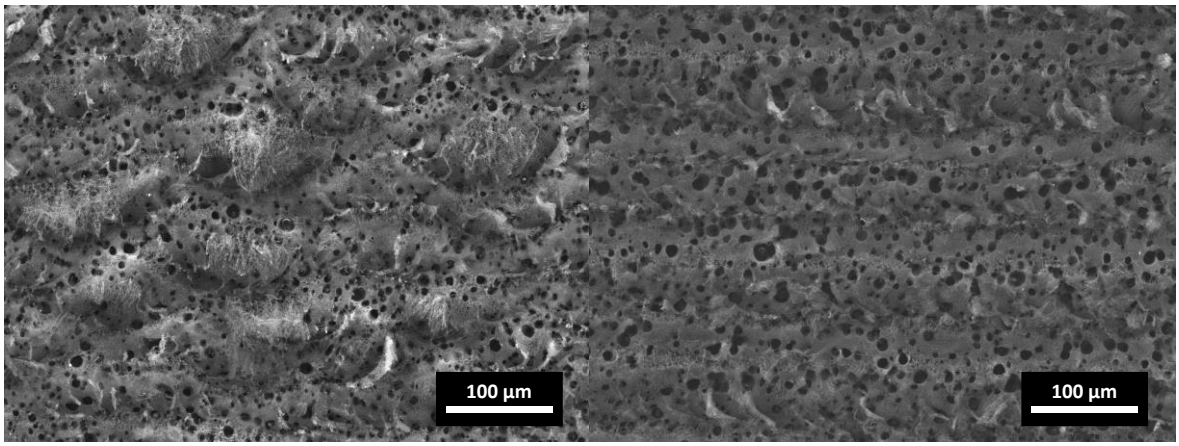

Figure 25: SEM images of a sample produced with a scan speed of 500 mm/s, 25 $\%P_{max}$ and 0.1 mm of distance between lines before (left) and after (right) being exposed to a constant water flow for five minutes.

In conclusion, the objective that was set in this section was achieved with success, having been reached an adequate laser parameter configuration: 100 mm/s of scan speed; 15 $\%P_{max}$ of power output, which corresponds to a laser power of 4.38 W; and a distance between lines of 0.1 mm. Having done that, LIG samples of 40×40 mm^2 in size, produced with these parameters were tested as electrodes in a CDI prototype (Section 6.3).

6.2 Commercial electrodes study

In this section, it is presented the characterization results, as well as its characterization, concerning the *Siontech*'s electrode, as well as the disassembly of this CDI module. Moreover, the results and analysis of three commercial electrodes are also presented, one from *Kuraray Company*, designated by Hard electrode, due to the presence of the graphite current collector already attached to the electrode material; and two electrodes from *MARKETECH International Inc.*, designated as Carbon paper grade I and II, depending on the surface area and porosity.

6.2.1 *Siontech*'s module disassembly

In a complementary way, a commercial CDI module from the *Siontech Company* was disassembled, in order to assess the cell's components and construction. The procedure followed is presented as it follows:

1. The adhesive tape present on the top face of the structure was removed. Initially, only the adhesive tape on hole one was removed;
2. The water stored inside the module was removed through hole one, and stored in a plastic cup. This water accounted for 100 ml, and contained some black particles in suspension;
3. The adhesive tape on hole two was removed;
4. Both circular nuts of the screws who served as the positive and negative contacts were removed, while maintaining the screws intact;
5. All the six circular nuts present on the top of the structure were removed, being that the first one was the nut in the right upper corner, followed by the rest in star order;
6. Carefully, the prototype was lifted, and the circular nuts of the bottom face remained on the table;
7. The screw that connected the top and bottom parts of the structure were removed;
8. Smoothly, the top part of structure was lifted (from this moment on, the handling of all the module components was done with the use of protection gloves);
9. The mini-Orings present on the screws were removed;
10. All the components responsible for the water desalination were removed from inside the structure aforementioned. Yet, one layer of the desalination structure remained, since it was partially damaged;
11. The screws that served has contacts were taken out;
12. The desalination structure was flipped upside down;
13. The screws that held together both brass structures were removed (the brass was held with our hands while the screws were removed);
14. Two small brass components were taken out, which showed the existence of some kind of resin which contributed for their adhesion. The second component being removed was the one connected to the layer of the desalination system that was partially damaged (step 10);
15. Finally, we proceeded to the counting and identification of all the different components of the desalination system, being composed of two plastic layers (at the top and bottom), forty-three electrodes (black layers) and forty-two spacers (clear layers);

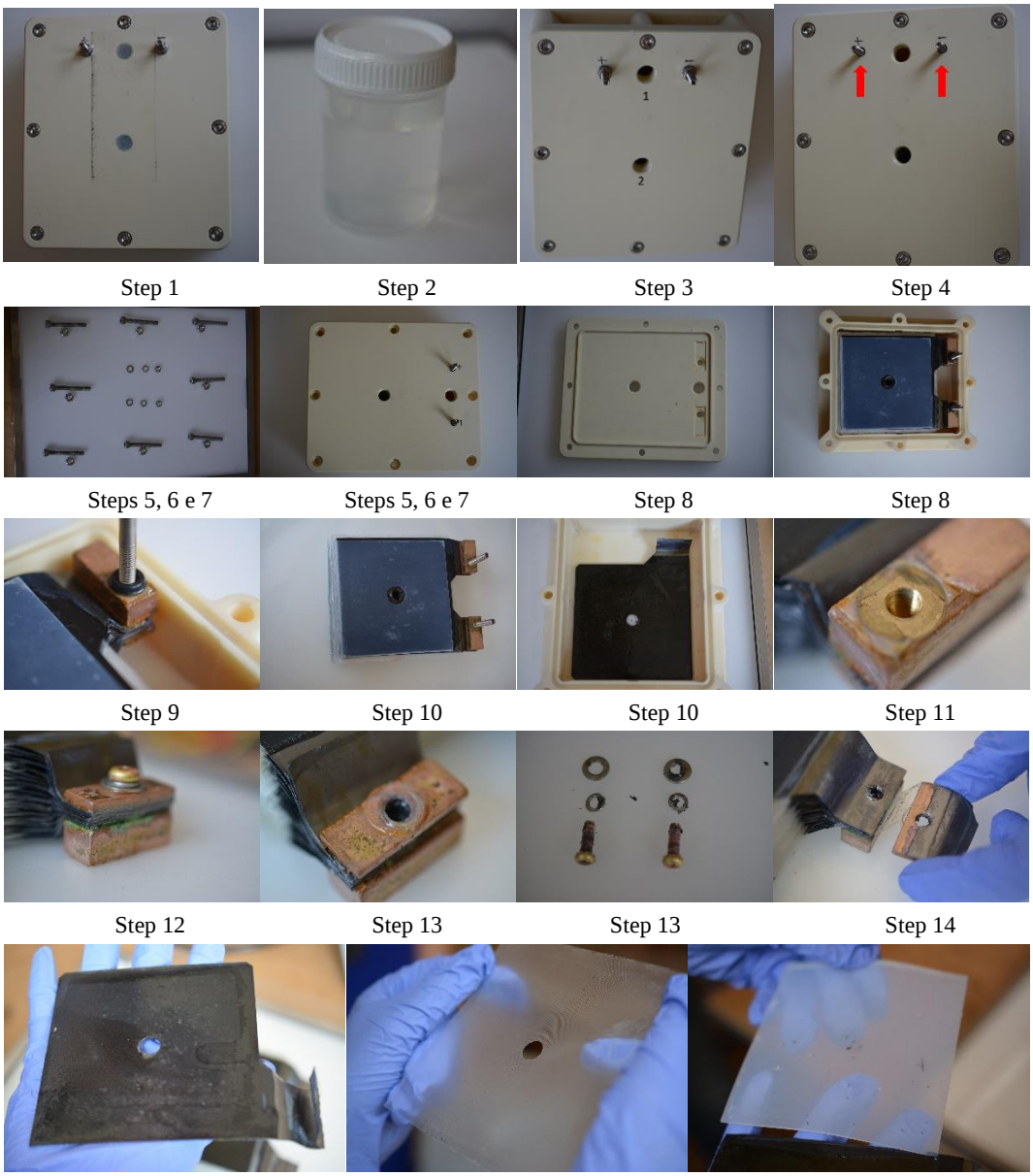

Figure 26: Disassembly sequence of the *Siontech*'s CDI module.

Afterwards, an example of an electrode, a spacer and plastic layer were removed from the rest, and proceeded to its characterization, via SEM and Raman spectroscopy.

6.2.2 *Siontech*'s electrode characterization

After completing the disassembly of the *Siontech*'s CDI module (Section 5.2), the characterization of its electrode was done. Firstly, Raman spectroscopy was performed in order to identify the materials composing them, Fig. 27. Notice that the green circle represents the contact zone between the electrode material (blue circle), and the current collector, (red circle).

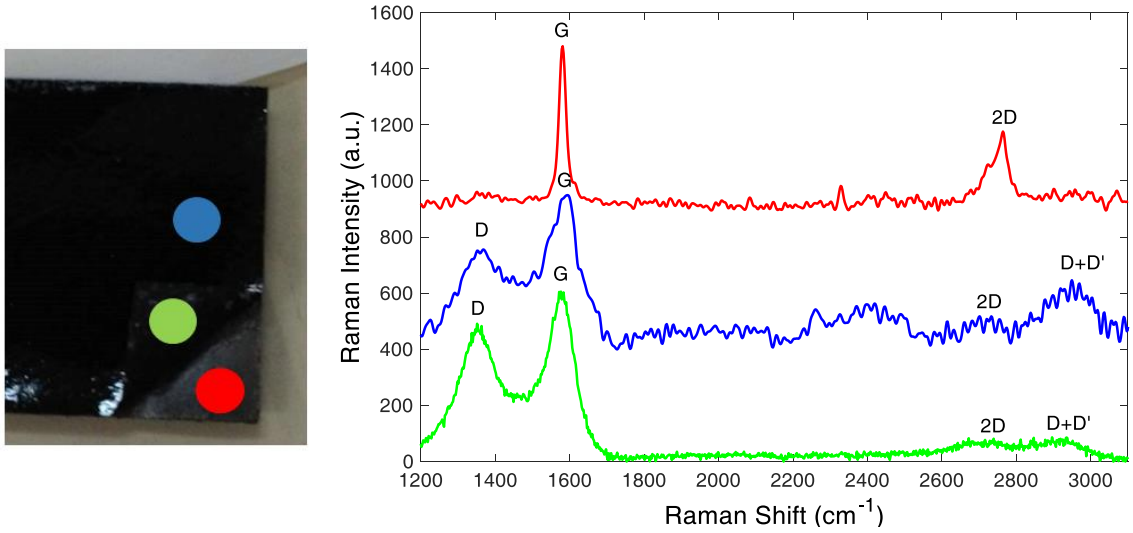

Figure 27: (left) Picture of the *Siontech*'s electrode, where the circles are the zones where the Raman spectra where taken; (right) Raman spectra of the marked areas on the Siontech's electrode.

From these spectra, we were able to identify that the electrode's material responsible for the deionization are activated carbon (blue and green spectra), while a graphite layer (red spectrum) is used for contact purposes [78].

Afterwards, the features of the electrode (Fig. 27 - left) were studied with SEM and EDS. The SEM images showed a very uniform porous surface (Fig. 28 - left), with micrometric particles. On the other hand, EDS analysis showed the presence of carbon together with various elements that were not expected. It showed the presence of Na and Cl on the activated carbon, stored there possibly due to the preliminary tests performed on the module. In addition, it was also found Br on the activated carbon, which has been used in water treatment techniques for its ability to kill harmful contaminants [79].

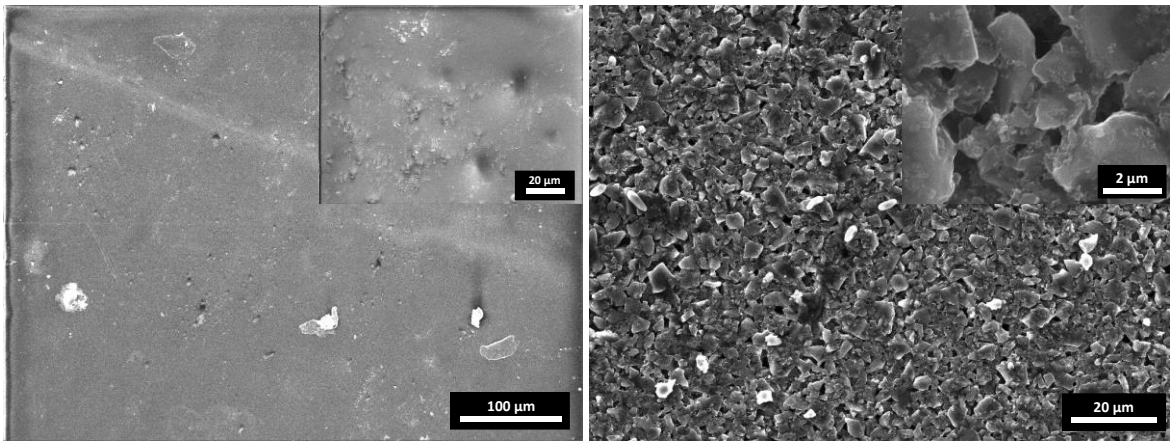

Figure 28: SEM images of (left) the *Siontech*'s electrode and (right) the *Kuraray*'s one.

To conclude the characterization, BET analysis was also performed, which showed that the activated carbon had a specific surface are of 544.93 m^2/g and an average pore size of 2.21 nm.

6.2.3 *Bosch* provided electrodes' characterization

After concluding the characterization of the *Siontech*'s electrode, a similar procedure was followed for the commercial electrodes provided by *Bosch*..

The electrode from *Kuraray* is designed in a similar way as the one from *Siontech*, since the current collector is already attached to the electrode material (Fig. 29 - left). In fact, Raman spectroscopy proved that the material responsible for the deionization process was an activated carbon, while the current collector was composed by graphite [78] (Fig. 29 - right).

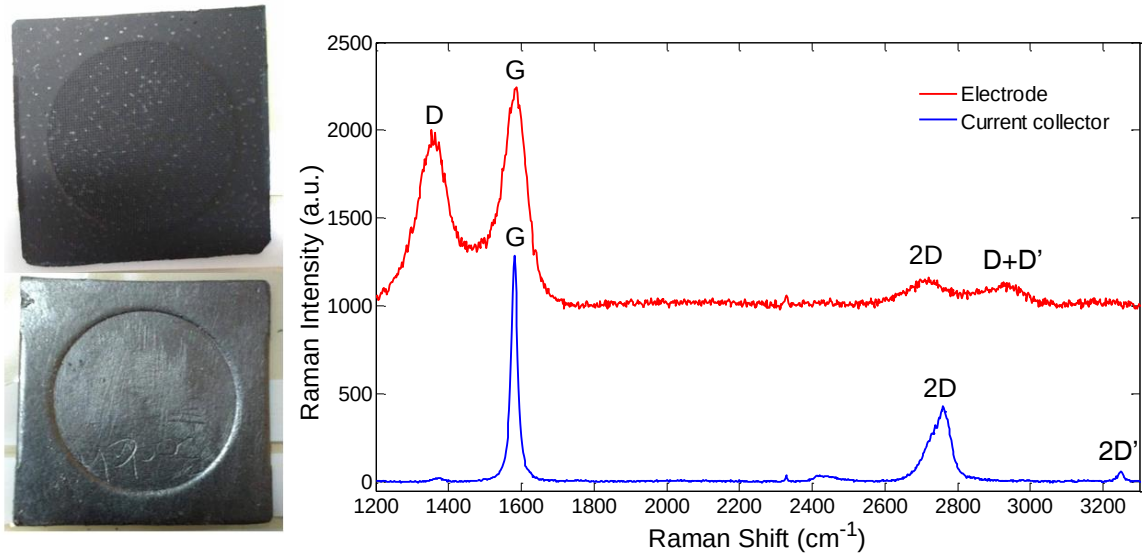

Figure 29: (left) *Kuraray*'s electrode, being the top picture the activated carbon side and the bottom picture the graphite side (current collector); (right) Raman spectra of both the material composing the electrode.

After the Raman spectroscopy characterization was complete, SEM imaging was done. Unlike the *Siontech*'s electrode, the SEM images obtained for the *Kuraray*'s electrode revealed a rougher surface morphology (at least considering the limits of the microscope used), which is more adequate for the application in mind. Looking at them (Fig. 28 - right), it can be seen a surface that appears to

have higher specific surface area compared to the other company's electrode material. This was confirmed once a sample of this electrode was analysed via BET, obtaining a specific surface area of 1160.92 m^2/g and an average pore size of 2.31 nm.

Comparing the *Kuraray* and the *Siontech*'s electrodes, it is clear that the one which possesses the most suitable activated carbon for CDI is the *Kuraray*. This comes from, despite having similar average pore sizes, the *Kuraray*'s electrode exhibits a much larger surface area and pore volume. In fact, the results obtained for this electrode are in agreement to activated carbons found in the literature [80]. However, is has already been reported activated carbons with superior values of surface area, up to twice the value obtained for the *Kuraray*'s, due to different types of doping [81,82]. These high values of surface area found across the literature confirm the lower quality of the activated carbon found on the *Siontech*'s electrode.

Finally, the last two commercial electrode materials being characterized were two carbon papers, from *MARKETECH International Inc.*, and provided by *Bosch*. In this work, they were differentiated by naming them "carbon paper I" and "carbon paper II", the latter being expected to have higher specific area, by indication of the supplier.

Once again, Raman spectroscopy and SEM imaging were the characterization techniques employed. From Raman spectroscopy, it was possible to identify the type of carbon that these materials where composed of, being confirmed that both papers are also activated carbons [78] (Fig. 30 - left). On the other hand, SEM images showed an interesting surface morphology with a significantly different appearance when compared with the previous materials (Fig. 30 - right). On both the carbon papers, the surface did not seem to be optimal for CDI applications, since it seemed a very smooth solid surface with very low porosity. However, numerous cracks can be seen on the materials' surface. Upon closer look at these regions, we were able to verify the existence of a porous structure, which makes it possible to be applied in CDI applications (inset of Fig. 30 - right). In fact, the BET analysis revealed that the average pore size from Carbon paper I was 3.38 nm, while Carbon paper II had an average pore size of 10.08 nm. However, the specific surface area obtained for these materials were of 3.03 m^2/g for Carbon paper I and 137.83 m^2/g for Carbon paper II, which strongly contrasts from the expected values of ~400 m^2/g for Carbon paper I and ~600 m^2/g for Carbon paper II, according to the supplier's information. Even the average pore size presents a significant difference from the ones provided by the supplier, since values of ~60 nm and ~75-80 nm are reported from the Carbon papers I and I, respectively. These differences can be explained if the supplier's analysis were performed prior to the assembly of the raw activated carbon as free-standing electrode, since this assembly usually involves the addition of binder materials that may obstruct the pores and reduced the surface area. Moreover, it is important to take into account that, in the present study, the method considered the whole mass of the material to calculate the surface area, and not only the area of the material that participates in the CDI process, since, in the case of the Carbon papers only the pores inside the cracks engage in the deionization.

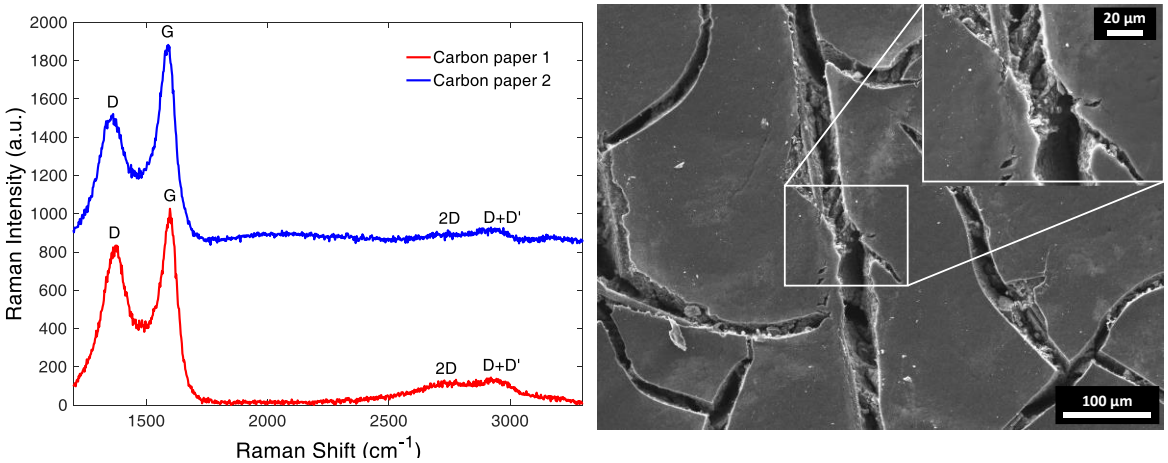

Figure 30: (left) Raman spectra obtained for both the carbon papers and (right) a SEM image of Carbon paper I highlighting the pores in the cracks.

6.3 CDI results

6.3.1 Testing prototype

Before applying the LIG electrodes on the testing prototype, measuring tests were performed on the conductivity meter to obtain the calibration curve. For these tests, several water samples with different salt concentrations were used, and upon applying a voltage 1 V AC, the voltage between the graphite electrodes was measured. These results can be found on Fig. 31.

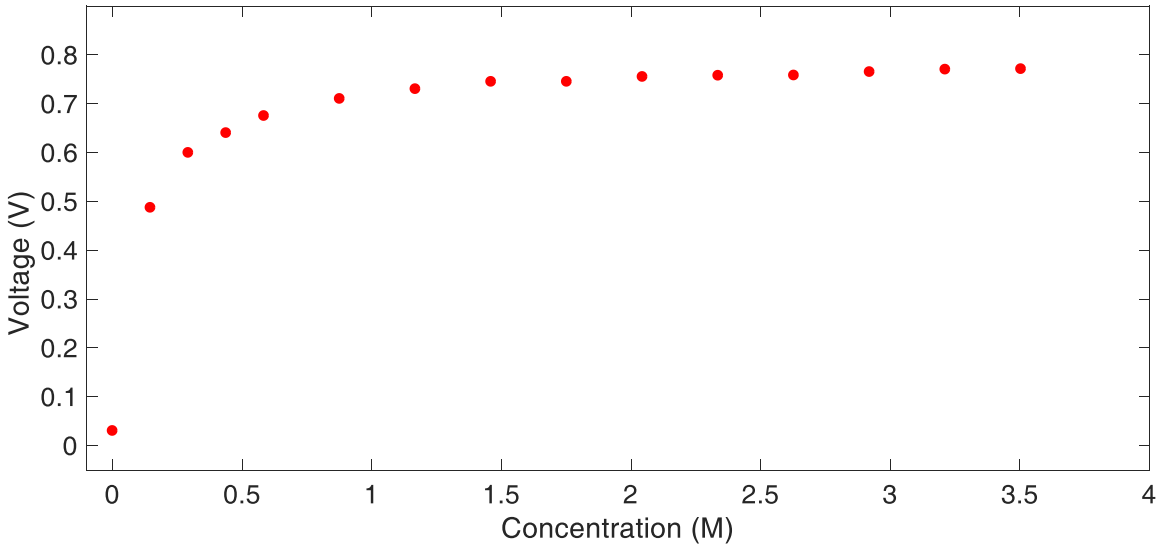

Figure 31: Plot of the potential values obtain for different salt concentrations using the conductivity meter.

From these results, it is possible to conclude that our conductivity meter works, at least with standing water, since it measures higher values of potential for higher concentrations, reaching saturation for concentrations values over 1 M. For this reason, the salt concentrations used in the experiments were always inferior to 1 M.

The CDI geometry used in the *Bosch*'s module resembled a flow-by mode (Fig. 5a), as in the case of the one from *Siontech*. Not to mention, while the previous module presented a deionization structure comprising many layers, the testing prototype is only composed of a pair of electrodes (positive and negative) and a spacer, and was created to experiment electrodes of different materials. In this prototype, the electrical voltage is applied via a brass piece in contact with a current collector, which is attached to the electrode using a binder

However, once the CDI tests began, no variation on the conductivity was observed. No difference was perceived, which would be expected once the potential was applied on the prototype. This raised some questions on whether our electrode's material would be adequate for CDI application, or if our conductivity meter could not perform measurements on a constant water flow. Yet, after reopening the prototype, it was seen that the main problem was the smashing of the electrodes, because the space between the brass contacts was smaller than the combined thickness of both electrodes and the spacer, not allowing the water stream to flow through them (Fig. 32). From here, it was concluded that the prototype could not be used, propelling the idealization of a different experimental set up (subsection 5.3) to evaluate the deionization capabilities of both our material as well as the commercial (*Kuraray* and *Siontech*'s electrodes) materials.

Figure 32: Photographs of the (left) spacer and (right) one of the LIG electrodes used in the testing prototype.

6.3.2 CDI studies

Since the experimental apparatus using the testing prototype did not show conclusive results concerning the CDI capabilities of our electrode, another set up was conceived (subsection 5.3.2). Once again, the conductivity measurements were not possible to be conducted. Hence, only the charge and discharge cycles of the electrodes were determined, in both modes of constant voltage and current.

Firstly, measurements in the CV-mode where performed for each of the electrodes considered: the LIG electrode; *Kuraray*'s electrode and the electrode retrieved from the *Siontech*'s module. Hence, the integrated areas of all the curves obtained in the CV-mode were calculated between 90% and 10% of the full charge. This way, it was ensured the comparison between all the electrodes' results. For each of the considered electrodes, it was determined the integrated area under the current vs time curves, as well as the time it took for the charge and the discharge to occur. These results can

be found in Table 8 (the numbers “1”, “2” and “3” correspond to the charge/discharge cycles obtained for each electrode material).

Table 8: Results obtained from the analysis of the current over time curves in the CV-mode experiments.

Electrode	Area (C)						Time (s)								
	Charge			Discharge			Charge			Discharge			Cycle		
	1	2	3	1	2	3	1	2	3	1	2	3	1	2	3
LIG	0.069	0.073	0.073	0.052	0.041	0.042	54.25	61.76	77.17	26.71	47.73	59.09	80.96	109.49	136.26
Kuraray	7.44	6.180	-	5.49	5.98	-	507.56	395.16	-	331.72	378.10	-	839.28	773.26	-
Siontech	2.23	2.29	2.63	2.28	2.67	2.50	63.40	65.02	87.76	69.15	86.92	104.56	132.55	151.94	192.32

At this point, some conclusions can be drawn from the CV-mode experiments. Firstly, both the LIG and *Siontech*’s electrodes had relatively short charge and discharge cycles when compared to the *Kuraray*’s one, which had cycles up to six times longer. The longer duration of these cycles can be considered a desired feature when it comes to CDI applications, since it facilitates the process for lowering the frequency at which the effluent water concentration varies. However, it is not as important as the number of ions that are removed for the water. To evaluate this feature, the integrated areas obtained are used, which correspond to the accumulated charge in the electrodes. In order to compare the electrodes, it is considered an operation time of 16000 s (charge time plus discharge time), where the *Kuraray*’s, *Siontech*’s and LIG electrodes showed an accumulated charge of 138.4 C, 240.0 C and 10.5 C, respectively. This shows that, for equal operation time, the *Siontech*’s electrode seems to be the most adequate in the CV-mode.

Furthermore, all the electrodes’ curves (Fig. 33) had a common feature amongst them, which was the fact that the discharge portion of the cycle was faster than the charge one.

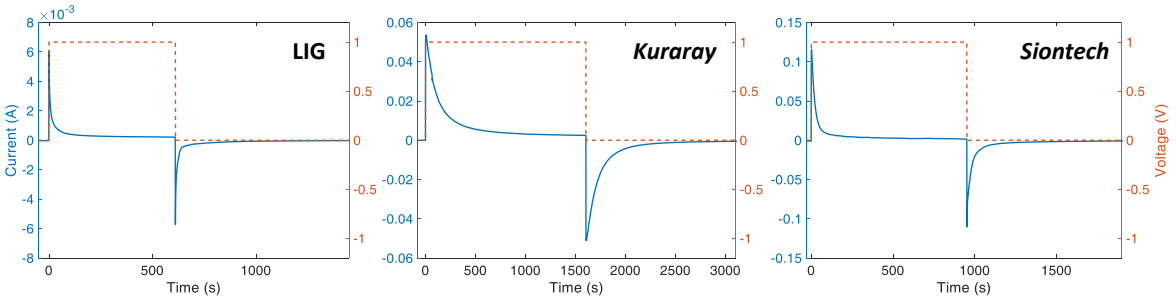

Figure 33: Cycles number 2 obtained in the CV-mode for the studied electrodes.

However, these experiments using the CV-mode also showed a common occurrence for all the electrodes. After the first cycle, the peak values would decrease from cycle to cycle (Fig. 34 - left). This situation is not at all desired, since it indicates that the quantity of ions that are accumulated on the electrodes varies throughout its usage. Adding to this issue, the charge and discharge times also vary. This can be explained by the fact that only three CDI cycles were performed for each electrode, which is not enough for the electrodes to reach the dynamic equilibrium. Uncharged carbons can adsorb salt without the application of a voltage, making the first cycles important to expel this initial

ions stored in the pores, which is why it is important to run a few cycles before the system being able to obtain more accurate results [31,83]. Moreover, in the first cycles, the electrodes may not be fully wetted, worsening the electrode's performance. Meanwhile, the lack of control and stability of the quantity of salt that is removed from the water is another issue of the CV-mode, when commercial applications are in mind, since a control of the salt concentration during the operation time is desired (Fig. 34 - right) [4].

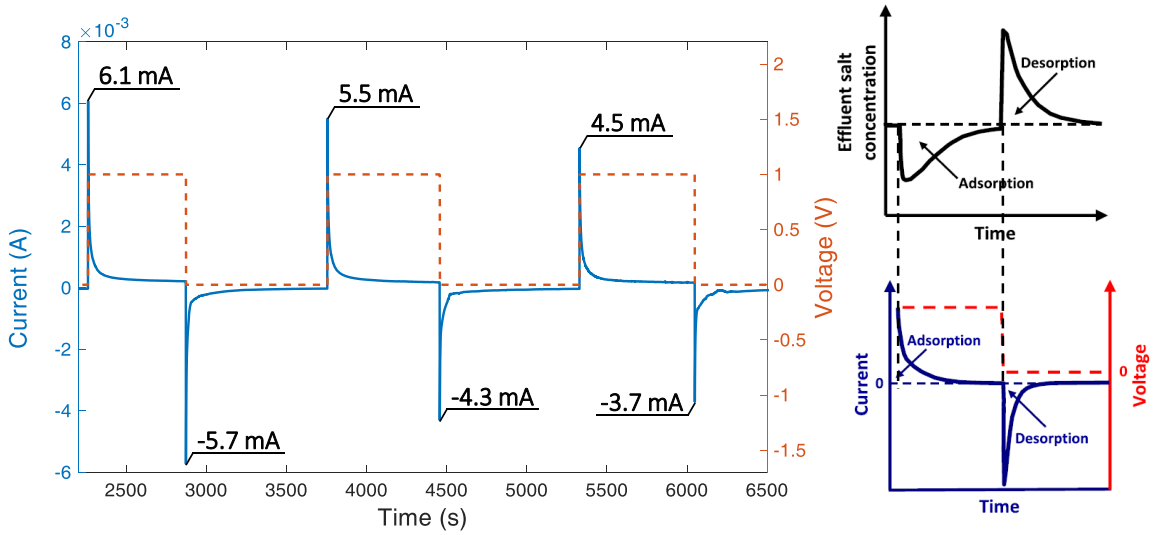

Figure 34: (left) Current and voltage over time curves obtained for the LIG electrode in the CV-mode and (right) the expected current vs time curves, as well as the CDI cycles for the CV-mode [4].

Upon these conclusions, the CC-mode was studied with the same electrodes. Using this operation mode, the ion adsorption occurs at a constant pace. In this mode, the quantity of salt adsorbed by the electrodes steadily increases throughout the time where the current is being applied, up until it is reversed. Once this happens, the desorption stage shows a constant value of salt concentration of the effluent (Fig. 7 in subsection 2.2.3). Thus, possibly the main advantage of working in CC-mode over the CV-mode is the better control throughout the deionization process.

The curves analysis' results are found in Table 9 (notice that in this mode, the "Area" still corresponds to the integrated area under the curve of the current over time). So, in order to compare the *Siontech* and *Kuraray* electrodes' results with those of LIG, the time was multiplied by five, assuming a charge and discharge operation at 1 mA.

Table 9: Results obtained from the analysis of the current over time curves in the CC-mode experiments.

Electrode	Area (C)						Time (s)								
	Charge			Discharge			Charge			Discharge			Cycle		
	1	2	3	1	2	3	1	2	3	1	2	3	1	2	3
LIG	0.0072	0.0064	0.0062	0.005	0.0049	0.0048	47	42	41	33	33	32	81	75	73
Kuraray	8.67	8.77	7.50	7.09	6.04	6.60	8668	8768	7504	7093	6041	6603	15761	14584	14107
Siontech	3.06	3.34	3.22	3.00	2.84	2.77	3063	3340	3218	2995	2843	2772	6059	6184	5991

Once again, the *Kuraray*'s electrode was the one with the longest cycle time. However, the difference between the *Siontech*'s and the LIG is more accentuated, compared to the difference seen between these electrodes in the CV-mode. Besides, both the commercial electrodes showed the ability to operate for considerably longer periods of time in the CC-mode. However, this feature is not as relevant as the accumulated charge for the same time span. Looking at Table 10, we can notice that for the same period of operation time of 16000 s, the accumulated charge obtained in the CV-mode is higher, which points to higher salt adsorption. On the other hand, in the case of the *Kuraray* and *Siontech*'s electrodes, it is required fewer cycles to achieve the same accumulated charge. In the CC-mode, the *Kuraray*'s electrode would require 17.0 cycles to achieve an accumulated charge of 138.4 C, while the Siontech's electrode would only need 73.8 cycles to accumulate a charge of 240.0 C. This can be seen as an advantage if the operation apparatus is very complex, since it lowers the amount of times the effluent alternates between deionized water and overconcentrated water. Yet, in the case of the LIG, the scenario is the complete opposite, where not only the accumulated charge in the CC-mode is lower compared to the CV-mode, but it also required many more operation cycles in the CC-mode to achieve the same adsorption amount as in the CV-mode.

Table 10: Comparison between the CV-mode and the CC-mode for an operation time of 16000 s.

Electrode	CV-mode		CC-mode	
	Accumulated charge (C)	Number of cycles	Accumulated charge (C)	Number of cycles
LIG	10.5	146.9	1.38	209.6
Kuraray	138.4	19.8	8.97	1.1
Siontech	240.0	100.7	8.45	2.6

Indeed, the difference between the accumulated charge between the electrodes in the CV-mode can possibly arise from several features, not only from the physical properties of the electrodes, but also from experimental apparatus. Firstly, the fact that the LIG electrode exhibits the lowest accumulated charge of the three is expected, since it was the one with the lowest value of surface area, according to the BET measurements. Moreover, the highest average pore size measured for these electrodes, and according to the literature, pore sizes of <2 nm are more beneficial for slat adsorption [31]. On the other hand, the *Siontech*'s electrode would accumulate more charge within

the same operation time as the *Kuraray*'s, despite having a considerably lower surface area. This can be explained by the fact that, in the case of the *Siontech*'s electrode, activated carbon can be found on both sides of it, being the graphite current collector placed in the middle, while in the *Kuraray*'s, the material responsible for the deionization can only be found in the face exposed to the water. Even though the electrodes were fixed to microscope blades, some water could be found between the blade and the electrode, causing the *Siontech*'s electrode to have twice the contact area compared to the other two electrodes.

In the CC-mode, the differences between the accumulated charges for the electrodes for an operation time of 16000 s are certainly distinct from the difference seen in the CV-mode. Even though the LIG electrode continues to show the smallest value of accumulated charge, the other two electrodes showed similar values of this parameter. This can be accounted by the current applied to the electrodes in this mode. From the CV-mode plots (Fig. 33), we can notice that, the maximum current value reached for the *Siontech*'s electrode was of 116.4 mA, 50.9 mA for the *Kuraray*'s and 5.4 mA for the LIG electrode (since current peaks vary from cycle to cycle, these values correspond to the average of the first 3 cycles of each electrode). On the other hand, in the CC-mode experiments, the electrodes were subjected to currents of 1 mA (LIG) and 5 mA (*Siontech* and *Kuraray*), which is lower than the maximum observed in the CV-mode experiments. Beginning with the LIG, we can calculate that the current applied is approximately 18.5 % of the maximum current. However, in order to compare these results accurately with those obtained in the CV-mode, all the accumulated charges in the CC-mode should be calculated considering that the same percentage of maximum current is applied in each electrode. So, the accumulated charges for each electrode were recalculated considering that the current applied to each electrode was 18.5 % of the maximum current. These corrections are in Table 11:

Table 11: Comparison between the accumulated charge in the CV-mode and CC-mode, while applying the 18.5% of the maximum current correction in the latter mode.

Electrode	Accumulated charge in the CV-mode (C)	Accumulated charge in the CC-mode (C)
LIG	10.5	1.38
Kuraray	138.4	18.43
Siontech	240.0	39.08

From the values in Table 11, we can calculate the charge ratio between electrodes within each mode. In the case of the CV-mode, the LIG electrode accumulates 13.18 times less charge than the *Kuraray*'s, while in the CC-mode, accumulates a value of 13.36 was obtained for the same comparison. For the charge ration between the Kuraray's and the *Siontech*'s, in the CV-mode, the *Siontech*'s accumulates 2.12 times more than the *Kuraray*'s, and 1.73 times more in the CC-mode. This shows that, even varying the current supplied to the electrodes in the CC-mode, the difference between them is similar to that seen in the CV-mode, as long as the same percentage of the maximum current is kept.

Also, looking at the plots in Fig. 35, it is noticeable the difference in the shape of the curves between the commercial electrodes and LIG. In the case of LIG, in both the charge and the discharge parcels of the cycle, the curves are a lot smoother when compared to the other two electrodes. We believe that this is derived from the fact that both of the commercial electrodes were tested in lower percentages of their maximum current.

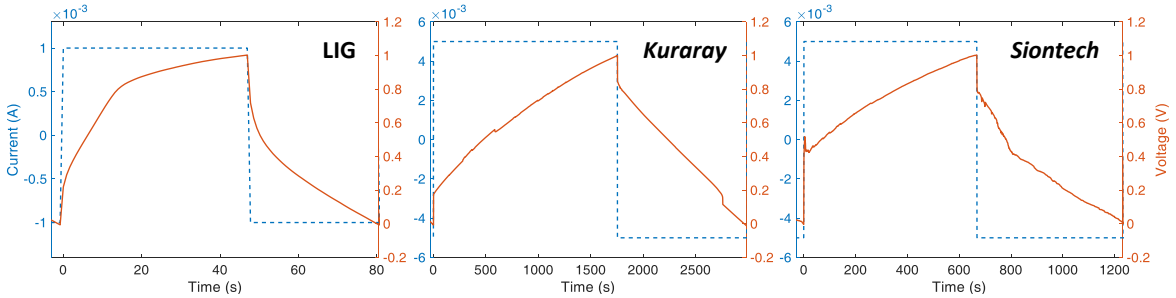

Figure 35: Cycles number 2 obtained in the CC-mode for the studied electrodes.

From this study, it was possible to conclude that, between the CV-mode and the CC-mode, our electrode operates better in the former, exhibiting higher charge accumulation with less operating cycles, considering the applied currents. On the other hand, the results from the other two electrodes did not evidence a clear-cut preference from each of the operating modes. Both commercial electrodes showed good features in each of the modes. The higher amount of accumulated charge per time was obtained with the CV-mode (for the currents used), while a lower number of cycles to achieve the same number of ions adsorbed was evidenced in the CC-mode. In fact, the decisive factor when choosing between both of this operation modes could be the system's apparatus, where the higher number of cycles needed in the CV-mode could present a considerable issue. However, and especially in the case of the *Kuraray* and *Siontech*'s electrodes, if the parameters studied in this work (accumulated charge and operation time) are similar between both modes, the CC-mode should be the preferred one, for its better control of the water concentration leaving the CDI cell (Subsection 2.2.3).

Nevertheless, it was shown that the LIG produced electrode still has some limitations when compared to the other two materials studied in this work. Not only it exhibited lower charge accumulation, but also had very short cycles, presenting added experimental difficulties to implement this material in a commercial device. This can be attributed to the lower surface area and the larger pore size in the LIG material. Another parameter that could limit the LIG's performance is the surface's wettability, which can hinder ion adsorption. In addition, the absence of a current collector leads to potential drops across the electrode, thus reducing the CDI performance.

7. Conclusions and future work

In this work, the initial goal of developing a laser grown graphene-based material was achieved with success. Through its characterization via SEM, Raman spectroscopy, BET analysis, Van der Pauw sheet resistance measurements and water stability tests, we were able to reach the most adequate laser parameter combination for the produced laser induced graphene (LIG): scan speed of 100 $\mathrm{mm/s}$, laser power of 15 $\%P_{max}$ and a distance between laser lines of 0.1 mm. In addition, similar morphological characterization was performed in four commercial electrodes: *Kuraray*'s, Siontech's and *MARKETECH*'s (Carbon papers I and II). From these studies, it was possible to identify all of them as being composed of activated carbon, and in the case of the *Kuraray*'s and the *Siontech*'s, a graphite current collector was used to enhance the electrode's electrical conductivity, since the activated carbon has a low value for this property. These studies allowed us to conclude that the *Kuraray*'s electrode was clearly the most suitable for capacitive deionization (CDI) application, mainly due to its far superior surface area compared to the remaining.

Throughout the CDI experiments, we were able to conclude, based on the duration of the charge/discharge cycles, that the CV operation mode was more adequate than the CC-mode for the LIG electrodes. On the other hand, for the commercial electrodes there were advantages and disadvantages in both modes, and in order to assess which one is better, further studies are required.

For future work, it is relevant to conduct several additional studies, envisaging both the understanding and the enhancement of the LIG's performance:

- To investigate methods to improve the pore size as well as the specific surface area of the LIG;
- To modify the LIG properties, for instance via addition of other materials (*e.g.* metals or oxides) in order to enhance the surface area;
- To improve the wettability of the LIG's surface, for example by functionalization, and induce ion selectivity;
- To develop a better experimental set up, namely to enable the conductivity measurements, as well as to control the contact areas between the electrodes and the water;
- To promote an upscale of the CDI system in order to achieve measurable conductivity changes;
- To perform durability and stress tests on the CDI system.

References

[1] A.T.A.S.N.M. Noel, Review on carbon-based electrode materials for application in capacitive deionization process, Int. J. Environ. Sci. Technol. 13 (2016) 2961–2976. doi:10.1007/s13762-016-1061-9.

[2] Y. Li, J. Shen, J. Li, X. Sun, J. Shen, W. Han, L. Wang, A protic salt-derived porous carbon for ef fi cient capacitive deionization : Balance between porous structure and chemical composition, Carbon N. Y. 116 (2017) 21–32. doi:10.1016/j.carbon.2017.01.084.

[3] J. Gabitto, C. Tsouris, Volume Averaging Study of the Capacitive Deionization Process in Homogeneous Porous Media, Transp. Porous Media. 109 (2015) 61–80. doi:10.1007/s11242-015-0502-0.

[4] S. Porada, R. Zhao, A. Van Der Wal, V. Presser, P.M. Biesheuvel, Progress in Materials Science Review on the science and technology of water desalination by capacitive deionization, Prog. Mater. Sci. 58 (2013) 1388–1442. doi:10.1016/j.pmatsci.2013.03.005.

[5] L.F. Greenlee, D.F. Lawler, B.D. Freeman, B. Marrot, P. Moulin, Reverse osmosis desalination: Water sources, technology, and today's challenges, Water Res. 43 (2009) 2317–2348. doi:10.1016/j.watres.2009.03.010.

[6] H. El-Dessouky, H.I. Shaban, H. Al-Ramadan, Steady-state analysis of multi-stage flash desalination process, Desalination. 103 (1995) 271–287. doi:10.1016/0011-9164(95)00080-1.

[7] N.H. Aly, A.K. El-Fiqi, Mechanical vapor compression desalination systems - A case study, Desalination. 158 (2003) 143–150. doi:10.1016/S0011-9164(03)00444-2.

[8] M. Al-Sahali, H. Ettouney, Developments in thermal desalination processes: Design, energy, and costing aspects, Desalination. 214 (2007) 227–240. doi:10.1016/j.desal.2006.08.020.

[9] M.A. Anderson, A.L. Cudero, J. Palma, Capacitive deionization as an electrochemical means of saving energy and delivering clean water. Comparison to present desalination practices: Will it compete?, Electrochim. Acta. 55 (2010) 3845–3856. doi:10.1016/j.electacta.2010.02.012.

[10] W. Kong, X. Duan, Y. Ge, H. Liu, J. Hu, X. Duan, Holey graphene hydrogel with in-plane pores for high- performance capacitive desalination, 9 (2016) 2458–2466. doi:10.1007/s12274-016-1132-8.

[11] J. Ma, D. He, W. Tang, P. Kovalsky, C. He, C. Zhang, T.D. Waite, Development of Redox-Active Flow Electrodes for High-Performance Capacitive Deionization, (2016). doi:10.1021/acs.est.6b03424.

[12] S. Burn, M. Hoang, D. Zarzo, F. Olewniak, E. Campos, B. Bolto, O. Barron, Desalination techniques - A review of the opportunities for desalination in agriculture, Desalination. 364 (2015) 2–16. doi:10.1016/j.desal.2015.01.041.

[13] H.B. Harandi, M. Rahnama, E. Jahanshahi Javaran, A. Asadi, Performance optimization of a multi stage flash desalination unit with thermal vapor compression using genetic algorithm, Appl. Therm. Eng. 123 (2017) 1106–1119. doi:10.1016/j.applthermaleng.2017.05.170.

[14] L. Han, K.G. Karthikeyan, M.A. Anderson, K.B. Gregory, Journal of Colloid and Interface Science Exploring the impact of pore size distribution on the performance of carbon electrodes for capacitive deionization, J. Colloid Interface Sci. 430 (2014) 93–99. doi:10.1016/j.jcis.2014.05.015.

[15] Y. Oren, Capacitive deionization (CDI) for desalination and water treatment — past , present and future (a review), 228 (2008) 10–29. doi:10.1016/j.desal.2007.08.005.

[16] S. Ahualli, G.R. Iglesias, M.M. Fernández, M.L. Jiménez, Á. V. Delgado, Use of Soft Electrodes in Capacitive Deionization of Solutions, Environ. Sci. Technol. (2017) acs.est.6b06181. doi:10.1021/acs.est.6b06181.

[17] V.A. Online, S. Porada, L. Borchardt, M. Oschatz, M. Bryjak, J.S. Atchison, K.J. Keesman, S. Kaskel, P.M. Biesheuvel, V. Presser, Environmental Science porous carbon electrodes for capacitive deionization †, (2013) 3700–3712. doi:10.1039/c3ee42209g.

[18] M. Aslan, M. Zeiger, N. J, I. Grobelsek, D. Weingarth, Improved capacitive deionization performance of mixed hydrophobic / hydrophilic activated carbon electrodes, 28 (2016). doi:10.1088/0953-8984/28/11/114003.

[19] B. Jia, W. Zhang, Preparation and Application of Electrodes in Capacitive Deionization (CDI): a State-of-Art Review, Nanoscale Res. Lett. (2016). doi:10.1186/s11671-016-1284-1.

[20] J.B. Park, W. Xiong, Y. Gao, M. Qian, Z.Q. Xie, M. Mitchell, Y.S. Zhou, G.H. Han, L. Jiang, Y.F. Lu, Fast growth of graphene patterns by laser direct writing, Cit. Appl. Phys. Lett. J. Laser Appl. 98 (2011). doi:10.2351/1.1771199.

[21] F. Wang, K. Wang, X. Dong, X. Mei, Applied Surface Science Formation of hierarchical porous graphene films with defects using a nanosecond laser on polyimide sheet, Appl. Surf. Sci. c (2017) 893–900. doi:10.1016/j.apsusc.2017.05.084.

[22] J. Lin, Z. Peng, Y. Liu, F. Ruiz-Zepeda, R. Ye, E.L.G. Samuel, M.J. Yacaman, B.I. Yakobson, J.M. Tour, Laser-induced porous graphene films from commercial polymers, Nat. Commun. 5 (2014) 1–8. doi:10.1038/ncomms6714.

[23] A. Lamberti, F. Perrucci, M. Caprioli, M. Serrapede, M. Fontana, S. Bianco, S. Ferrero, E. Tresso, New insights on laser induced graphene electrodes for flexible supercapacitors: tunable morphology and physical properties, Nanotechnology. (2017). doi:10.1088/1361-6528/aa6615.

[24] Y. Li, D.X. Luong, J. Zhang, Y.R. Tarkunde, C. Kittrell, F. Sargunaraj, Y. Ji, C.J. Arnusch, J.M. Tour, Laser-Induced Graphene in Controlled Atmospheres: From Superhydrophilic to Superhydrophobic Surfaces, Adv. Mater. 1700496 (2017) 1700496. doi:10.1002/adma.201700496.

[25] J.M. Chem, Carbon electrodes for capacitive deionization, J. Mater. Chem. A Mater. Energy Sustain. 5 (2016) 470–496. doi:10.1039/C6TA06733F.

[26] S. Jeon, H. Park, J. Yeo, S. Yang, C.H. Cho, M.H. Han, D.K. Kim, Desalination via a new membrane capacitive deionization process utilizing flow-electrodes, Energy Environ. Sci. 6 (2013) 1471–1475. doi:10.1039/c3ee24443a.

[27] J. Newman, R.G. Wilbourne, A.W. Venolia, A.M. Johnson, M. Company., U. States., The Electrosorb process for desalting water, (1970) iii, 31 . file://catalog.hathitrust.org/Record/005890599.

[28] K.B. Oldham, A Gouy-Chapman-Stern model of the double layer at a (metal)/(ionic liquid) interface, J. Electroanal. Chem. 613 (2008) 131–138. doi:10.1016/j.jelechem.2007.10.017.

[29] O. Stern, ZUR THEORIE DER ELEKTROLYTISCHEN DOPPELSCHICHT, Zeitschrift Für Elektrochemie Und Angew. Phys. Chemie. 30 (1924) 508–516. doi:10.1002/bbpc.192400182.

[30] P.M. Biesheuvel, H.V.M. Hamelers, M.E. Suss, Theory of Water Desalination by Porous Electrodes with Immobile Chemical Charge, Colloids Interface Sci. Commun. 9 (2015) 1–5. doi:10.1016/j.colcom.2015.12.001.

[31] M.E. Suss, S. Porada, X. Sun, P.M. Biesheuvel, J. Yoon, V. Presser, Water desalination via capacitive deionization: what is it and what can we expect from it?, Energy Environ. Sci. 8 (2015) 2296–2319. doi:10.1039/C5EE00519A.

[32] L. Han, K.G. Karthikeyan, K.B. Gregory, Energy Consumption and Recovery in Capacitive Deionization Using Nanoporous Activated Carbon Electrodes, 162 (2015) 282–288. doi:10.1149/2.0431512jes.

[33] A. Soffer, M. Folman, The electrical double layer of high surface porous carbon electrode, J. Electroanal. Chem. Interfacial Electrochem. 38 (1972) 25–43. doi:10.1016/S0022-0728(72)80087-1.

[34] A. Wo, Charge barrier flow-through capacitor, (2017) 1–10.

[35] E. Avraham, Y. Bouhadana, A. Soffer, D. Aurbach, Limitation of Charge Efficiency in Capacitive Deionization I. On the Behavior of Single Activated Carbon, J. Electrochem. Soc. 156 (2009) P95. doi:10.1149/1.3115463.

[36] G.S. Palacios, Electrode design and cell operation of a capacitive deionization system, Faculty 8 - Natural Sciences and Technology III of Saarland University, 2014.

[37] H. Li, Y. Gao, L. Pan, Y. Zhang, Y. Chen, Z. Sun, Electrosorptive desalination by carbon nanotubes and nanofibres electrodes and ion-exchange membranes, Water Res. 42 (2008) 4923–4928. doi:10.1016/j.watres.2008.09.026.

[38] Y.J. Kim, J.H. Choi, Selective removal of nitrate ion using a novel composite carbon electrode in capacitive deionization, Water Res. 46 (2012) 6033–6039. doi:10.1016/j.watres.2012.08.031.

[39] P.M. Biesheuvel, R. Zhao, S. Porada, A. van der Wal, Theory of membrane capacitive deionization including the effect of the electrode pore space, J. Colloid Interface Sci. 360 (2011) 239–248. doi:10.1016/j.jcis.2011.04.049.

[40] J.C. Farmer, S.M. Bahowick, J.E. Harrar, D. V Fix, R.E. Martinelli, A.K. Vu, K.L. Carroll, Electrosorption of Chromium Ions on Carbon Aerogel Electrodes as a Means of Remediating Ground Water, Energy & Fuels. 11 (1997) 337–347. doi:10.1021/ef9601374.

[41] R. Zhao, P.M. Biesheuvel, H. Miedema, H. Bruning, A. van der Wal, Charge efficiency: A functional tool to probe the double-layer structure inside of porous electrodes and application in the modeling of capacitive deionization, J. Phys. Chem. Lett. 1 (2010) 205–210. doi:10.1021/jz900154h.

[42] E. Bourcier, William L., Aines, Roger D., Haslam, Jeffery J., Schaldach, Charlene M., O'Brien, Kevin C., Cussler, Deionization and desalination using electrostatic ion pumping, 2011.

[43] S. Porada, B.B. Sales, H.V.M. Hamelers, P.M. Biesheuvel, Water desalination with wires, J. Phys. Chem. Lett. 3 (2012) 1613–1618. doi:10.1021/jz3005514.

[44] R. Zhao, P.M. Biesheuvel, a. van der Wal, Energy consumption and constant current operation in membrane capacitive deionization, Energy Environ. Sci. 5 (2012) 9520. doi:10.1039/c2ee21737f.

[45] Y. Liu, T. Lu, Z. Sun, D.H.C. Chua, L. Pan, Ultra-thin carbon nanofiber networks derived from bacterial cellulose for capacitive deionization, J. Mater. Chem. A. 3 (2015) 8693–8700. doi:10.1039/C5TA00435G.

[46] Z. Peng, D. Zhang, L. Shi, T. Yan, High performance ordered mesoporous carbon/carbon nanotube composite electrodes for capacitive deionization, J. Mater. Chem. 22 (2012) 6603. doi:10.1039/c2jm16735b.

[47] S. Porada, L. Weinstein, R. Dash, A. van der Wal, M. Bryjak, Y. Gogotsi, P.M. Biesheuvel, Water Desalination Using Capacitive Deionization with Microporous Carbon Electrodes, ACS Appl. Mater. Interfaces. 4 (2012) 1194–1199. doi:10.1021/am201683j.

[48] S. Porada, L. Borchardt, M. Oschatz, M. Bryjak, J.S. Atchison, K.J. Keesman, S. Kaskel, P.M. Biesheuvel Af, V. Presser, Direct prediction of the desalination performance of porous carbon electrodes for capacitive deionization, Energy Environ. Sci. Energy Environ. Sci. 6 (2013) 3700–3712. doi:10.1039/c3ee42209g.

[49] C.L. Mangun, K.R. Benak, J. Economy, K.L. Foster, Surface chemistry, pore sizes and adsorption properties of activated carbon fibers and precursors treated with ammonia, Carbon N. Y. 39 (2001) 1809–1820. doi:10.1016/S0008-6223(00)00319-5.

[50] C.M. Yang, W.H. Choi, B.K. Na, B.W. Cho, W.I. Cho, Capacitive deionization of NaCl solution with carbon aerogel-silicagel composite electrodes, Desalination. 174 (2005) 125–133. doi:10.1016/j.desal.2004.09.006.

[51] L. Li, L. Zou, H. Song, G. Morris, Ordered mesoporous carbons synthesized by a modified sol-gel process for electrosorptive removal of sodium chloride, Carbon N. Y. 47 (2009) 775–781. doi:10.1016/j.carbon.2008.11.012.

[52] D. Zhang, L. Shi, J. Fang, K. Dai, X. Li, Preparation and desalination performance of multiwall carbon nanotubes, Mater. Chem. Phys. 97 (2006) 415–419. doi:10.1016/j.matchemphys.2005.08.036.

[53] H. Li, L. Zou, L. Pan, Z. Sun, Novel graphene-like electrodes for capacitive deionization, Environ. Sci. Technol. 44 (2010) 8692–8697. doi:10.1021/es101888j.

[54] F. Stoeckli, A. Guillot, A.M. Slasli, D. Hugi-Cleary, Microporosity in carbon blacks, Carbon N. Y. 40 (2002) 211–215. doi:10.1016/S0008-6223(01)00176-2.

[55] D. Zhang, T. Yan, L. Shi, Z. Peng, X. Wen, J. Zhang, Enhanced capacitive deionization performance of graphene/carbon nanotube composites, J. Mater. Chem. 22 (2012) 14696. doi:10.1039/c2jm31393f.

[56] D. Zhang, T. Yan, L. Shi, Z. Peng, X. Wen, J. Zhang, Enhanced capacitive deionization of graphene/mesoporous carbon composites, Nanoscale. 22 (2012) 5440–5446. doi:10.1039/c2nr31154b.

[57] Dupont, DuPont ™ Kapton ®, Http://www.dupont.com/content/dam/dupont/products-and-Services/membranes-and-Films/polyimde-films/documents/DEC-Kapton-Summary-of-Properties.pdf. 50 (2012) 1–7. http://www.dupont.com/content/dam/dupont/products-and-services/membranes-and-films/polyimde-films/documents/DEC-Kapton-general-specs.pdf.

[58] L. Li, J. Zhang, Z. Peng, Y. Li, C. Gao, Y. Ji, R. Ye, N.D. Kim, Q. Zhong, Y. Yang, H. Fei, G. Ruan, J.M. Tour, High-Performance Pseudocapacitive Microsupercapacitors from Laser-Induced Graphene, Adv. Mater. 28 (2016) 838–845. doi:10.1002/adma.201503333.

[59] F. Clerici, M. Fontana, S. Bianco, M. Serrapede, F. Perrucci, S. Ferrero, E. Tresso, A.

Lamberti, In situ MoS2 Decoration of Laser-Induced Graphene as Flexible Supercapacitor Electrodes, ACS Appl. Mater. Interfaces. 8 (2016) 10459–10465. doi:10.1021/acsami.6b00808.

[60] S.P. Singh, Y. Li, A. Be'Er, Y. Oren, J.M. Tour, C.J. Arnusch, Laser-Induced Graphene Layers and Electrodes Prevents Microbial Fouling and Exerts Antimicrobial Action, ACS Appl. Mater. Interfaces. 9 (2017) 18238–18247. doi:10.1021/acsami.7b04863.

[61] V. Kochkodan, D.J. Johnson, N. Hilal, Polymeric membranes: Surface modification for minimizing (bio)colloidal fouling, Adv. Colloid Interface Sci. 206 (2014) 116–140. doi:10.1016/j.cis.2013.05.005.

[62] L.-Q. Tao, H. Tian, Y. Liu, Z.-Y. Ju, Y. Pang, Y.-Q. Chen, D.-Y. Wang, X.-G. Tian, J.-C. Yan, N.-Q. Deng, Y. Yang, T.-L. Ren, An intelligent artificial throat with sound-sensing ability based on laser induced graphene, Nat. Commun. 8 (2017) 14579. doi:10.1038/ncomms14579.

[63] A.C. Ferrari, Raman spectroscopy of graphene and graphite: Disorder, electron-phonon coupling, doping and nonadiabatic effects, Solid State Commun. 143 (2007) 47–57. doi:10.1016/j.ssc.2007.03.052.

[64] R.S. Das, Y.K. Agrawal, Raman spectroscopy: Recent advancements, techniques and applications, Vib. Spectrosc. 57 (2011) 163–176. doi:10.1016/j.vibspec.2011.08.003.

[65] A.C. Ferrari, D.M. Basko, Raman spectroscopy as a versatile tool for studying the properties of graphene, Nat. Publ. Gr. 8 (2013) 235–246. doi:10.1038/nnano.2013.46.

[66] P.W. Hawkers, J.C.H. Spence, Science of Microscopy, Volume I, Springer Science+Business Media, LLC, 2007.

[67] J. Banaszcyk, A. Schwarz, G. De Mey, V. Langenhove, The Van der Pauw method for sheet resistance measurements of polypyrrole-coated para-amide woven fabrics, J. Appl. Polym. Sci. 117 (2010) 2553–2558. doi:10.1002/app.

[68] S. Brunauer, P.H. Emmett, E. Teller, Adsorption of Gases in Multimolecular Layers, J. Am. Chem. Soc. 60 (1938) 309–319. doi:10.1021/ja01269a023.

[69] a. U. Dogan, M. Dogan, M. Onal, Y. Sarikaya, a. Aburub, D.E. Wurster, Baseline studies of the Clay Minerals Society source clays: Specific surface area by the BET method, Clays Clay Miner. 54 (2006) 62–66. doi:10.1346/CCMN.2006.0540108.

[70] K. Kaneko, C. Ishii, Superhigh surface area determination of microporous solids, Colloids and Surfaces. 67 (1992) 203–212. doi:10.1016/0166-6622(92)80299-H.

[71] P.S. Northrop, R.C. Flagan, G.R. Gavalas, Measurement of Gas Adsorption Isotherms by Continuous Adsorbate Addition, Langmuir. 3 (1987) 300–302. doi:10.1021/la00074a027.

[72] L.D. Gelb, K.E. Gubbins, Characterization of Porous Glasses: Simulation Models, Adsorption Isotherms, and the Brunauer−Emmett−Teller Analysis Method, Langmuir. 14 (1998) 2097–2111. doi:10.1021/la9710379.

[73] T.. Adinaveen, J.J.. Vijaya, L.J.. Kennedy, Comparative Study of Electrical Conductivity on Activated Carbons Prepared from Various Cellulose Materials, Arab. J. Sci. Eng. 41 (2016) 55–65. doi:10.1007/s13369-014-1516-6.

[74] H.R. Azimi, R. Taheri, Electrical conductivity of CuO nanofluids, Int. J.Nano Dimens. 6 (2015) 77–81.

[75] L.G. Cançado, A. Jorio, E.H.M. Ferreira, F. Stavale, C.A. Achete, R.B. Capaz, M.V.O. Moutinho, A. Lombardo, T.S. Kulmala, A.C. Ferrari, Quantifying defects in graphene via Raman spectroscopy at different excitation energies, Nano Lett. 11 (2011) 3190–3196. doi:10.1021/nl201432g.

[76] A.C. Ferrari, J.C. Meyer, V. Scardaci, C. Casiraghi, M. Lazzeri, F. Mauri, S. Piscanec, D. Jiang, K.S. Novoselov, S. Roth, A.K. Geim, Raman spectrum of graphene and graphene layers, Phys. Rev. Lett. 97 (2006) 1–4. doi:10.1103/PhysRevLett.97.187401.

[77] P.G. Spizzirri, J.H. Fang, S. Rubanov, E. Gauja, S. Prawer, Nano-Raman spectroscopy of silicon surfaces, Mater. Forum. 34 (2008) 161–166.

[78] A. Cuesta, P. Dhamelincourt, J. Laureyns, A. Martínez-Alonso, J.M.D. Tascón, Raman microprobe studies on carbon materials, Carbon N. Y. 32 (1994) 1523–1532. doi:10.1016/0008-6223(94)90148-1.

[79] M. Langsa, A. Heitz, C.A. Joll, U. Von Gunten, S. Allard, Mechanistic Aspects of the Formation of Adsorbable Organic Bromine during Chlorination of Bromide-containing Synthetic Waters, Environ. Sci. Technol. 51 (2017) 5146–5155. doi:10.1021/acs.est.7b00691.

[80] L. Zhang, Y. Liu, T. Lu, L. Pan, Cocoon derived nitrogen enriched activated carbon fiber networks for capacitive deionization, J. Electroanal. Chem. 804 (2017) 179–184. doi:10.1016/j.jelechem.2017.09.062.

[81] R.L. Zornitta, L.A.M. Ruotolo, Simultaneous analysis of electrosorption capacity and kinetics for CDI desalination using different electrode configurations, Chem. Eng. J. 332 (2018) 33–41. doi:https://doi.org/10.1016/j.cej.2017.09.067.

[82] A.S. Yasin, J. Jeong, I.M.A. Mohamed, C.H. Park, C.S. Kim, Fabrication of N-doped &SnO2-incorporated activated carbon to enhance desalination and bio-decontamination performance for capacitive deionization, J. Alloys Compd. 729 (2017) 764–775. doi:10.1016/j.jallcom.2017.09.185.

[83] P.M. Biesheuvel, S. Porada, M. Levi, M.Z. Bazant, Attractive forces in microporous carbon electrodes for capacitive deionization, J. Solid State Electrochem. 18 (2014) 1365–1376. doi:10.1007/s10008-014-2383-5.